

A Geometric Unification of Concept Learning with Concept Cones

Alexandre Rocchi-Henry^{*a} Thomas Fel^{*b} Gianni Franchi^a

^aU2IS Lab ENSTA Paris ^bKempner Institute, Harvard University

{alexandre.rocchi,gianni.franchi}@enstaparis.com

Abstract

Two traditions of interpretability have evolved side by side but seldom spoken to each other: Concept Bottleneck Models (CBMs), which prescribe what a concept should be, and Sparse Autoencoders (SAEs), which discover what concepts emerge. While CBMs use supervision to align activations with human-labeled concepts, SAEs rely on sparse coding to uncover emergent ones. We show that both paradigms instantiate the same geometric structure: each learns a set of linear directions in activation space whose nonnegative combinations form a concept cone. Supervised and unsupervised methods thus differ not in kind but in how they select this cone. Building on this view, we propose an operational bridge between the two paradigms. CBMs provide human-defined reference geometries, while SAEs can be evaluated by how well their learned cones approximate or contain those of CBMs. This containment framework yields quantitative metrics linking inductive biases – such as SAE type, sparsity, or expansion ratio – to emergence of plausible¹ concepts. Using these metrics, we uncover a “sweet spot” in both sparsity and expansion factor that maximizes both geometric and semantic alignment with CBM concepts.

Overall, our work unifies supervised and unsupervised concept discovery through a shared geometric framework, providing principled metrics to measure SAE progress and assess how well discovered concept align with plausible human concepts.

1. Introduction & Related Work

As artificial intelligence systems reach superhuman performance across diverse tasks [62, 86], understanding how

^{*} Equal contribution.

¹We adopt the terminology of Jacovi and Goldberg [47], who distinguish between *faithful* explanations (accurately reflecting model computations) and *plausible* explanations (aligning with human intuition and domain knowledge). CBM concepts are plausible by construction – selected or annotated by humans – though not necessarily faithful to the true latent factors that organise the data manifold.

they represent and manipulate information has become critical [1, 84]. Beyond scientific curiosity, interpretability is essential in safety-critical domains such as healthcare [97], autonomous driving [39], and scientific discovery [51], where trust and reliability depend on transparent decision-making [22, 36]. Vision models are no exception: with architectures like Vision Transformers [20, 23, 72, 104] achieving human-level perception, probing their internal structures has become a key research goal. Early attribution methods visualized regions influencing predictions [4, 27, 31, 67, 69, 85, 88, 90, 91, 93, 103], offering insight into where models attend but not what they represent. Later evaluations [15, 41, 46, 55, 68, 89] revealed that these methods capture only surface-level sensitivities, failing to expose the deeper structure of internal representations.

To address this, the field shifted toward concept-based interpretability [53, 79], which seeks semantically meaningful directions in representation space [7, 28, 29, 34, 38, 60, 61, 99, 106]. This perspective reframes interpretability from input attribution to understanding the geometry of learned features. While early work linked single neurons to concepts, later studies showed that neurons are polysemantic and basis-dependent [3, 25, 37], motivating a distributed view where concepts emerge as patterns in population activity rather than single-unit responses [29, 33, 106].

A theoretical framework for this distributed perspective emerged through the *Linear Representation Hypothesis* (LRH) [16, 25, 76], which posits that neural networks represent exponentially many features by encoding each as a sparse linear combination of neurons. Under this view, interpretability reduces to recovering the dictionary of directions that span the feature space [28]. This insight established a bridge between interpretability and classical dictionary learning [6, 24, 35]. Sparse autoencoders (SAEs) [9, 17, 49, 64] operationalize this principle by enforcing sparsity in an over-complete encoder–decoder architecture. When applied to large pretrained models such as DINOv2 [5, 18, 30, 72], SAEs uncover rich sets of recurring activation patterns, or *concepts*, that align with perceptual and functional features.

These developments repositioned interpretability around the structure of representations rather than surface-level explanations. However, the field has since bifurcated into two largely disjoint traditions. The first, exemplified by *Concept Bottleneck Models* (CBMs) [2, 11, 48, 52, 59, 66, 70, 71, 73, 94, 98, 102], follows the path of *interpretability by design*. CBMs embed human-defined concepts as intermediate variables within the model architecture, ensuring that predictions must flow through interpretable bottlenecks [59]. This approach enforces semantic alignment by supervision, allowing explicit reasoning about causal relations between concepts and outputs [21, 59]. Yet, it is constrained by the availability and completeness of labeled concept datasets, and by the rigidity of predefined concept taxonomies that may not reflect the structure of learned representations [19, 65].

The second tradition, represented by SAEs and related methods, embodies *interpretability by discovery*. Here, interpretability is not enforced but emerges from structure: the model learns a sparse dictionary whose atoms capture recurring directions in activation space [9, 17, 30, 50]. This approach scales naturally to foundation models [43, 72, 105], and has revealed a wealth of interpretable phenomena in large vision [29, 30, 60] and language models [9, 25, 95]. However, in the absence of supervision, unsupervised concept discovery faces a problem of non-identifiability [57, 58, 63]: infinitely many equivalent bases can reconstruct the same activations, and interpretability must then rely on emergent coherence rather than explicit alignment [74, 78].

Despite their shared goal of uncovering the latent structure of neural representations, CBMs and SAEs have evolved largely independently. Both assume that activations are organized by a few latent generative factors [13, 14, 26], but they differ in how they constrain this structure: CBMs rely on labeled concepts, while SAEs depend on sparse coding and reconstruction. Each thus regularizes the same conceptual space in a distinct way—semantic for CBMs and statistical for SAEs.

In this work,

- we show that both approaches can be viewed as two forms of dictionary learning: each decomposes activations into concept vectors and corresponding codes, but under different constraints—supervision versus sparsity. This shared view defines an *operational bridge* between them, where the CBM dictionary provides a reference for evaluating the concepts discovered by SAEs.
- we propose a set of quantitative metrics to measure this relationship, assessing how much the SAE’s learned concepts overlap with those of a CBM. Through extensive benchmarks, we analyze how key factors such as sparsity, dictionary size, and expansion ratio influence this alignment. Our results reveal a “sweet spot” of parsimony where SAEs best capture CBM-like representations.
- We put this framework into practice, showing that it yields



Figure 1. **Illustration of the concept learning spaces.** Each image $\mathbf{x} \in \mathcal{X}$ comes from hidden factors $\mathbf{c} \in \mathcal{C}$ through a generative process $\mathbf{G} : \mathcal{C} \rightarrow \mathcal{X}$. A neural network $\mathbf{f} : \mathcal{X} \rightarrow \mathcal{A}$ maps inputs to activations $\mathbf{a} = \mathbf{f}(\mathbf{x})$. Concept extraction aims to find a function $\mathbf{H} : \mathcal{A} \rightarrow \mathcal{C}$ that recovers these hidden factors. Here, \mathcal{C} is the *concept space* with interpretable axes (e.g., *rabbit*, *tree*), \mathcal{X} is the *input space* of images, and \mathcal{A} is the *activation space* where concepts can be linearly decoded.

actionable insights into how inductive biases shape interpretability. The CBM dictionary can inform the design and evaluation of SAEs, guiding the selection of key hyperparameters such as dictionary size, sparsity level k , and expansion factor, and offering a measurable signal of desirable concept emergence. Conversely, SAEs can reveal which concept structures emerge spontaneously under minimal assumptions, highlighting the inductive biases that favor the discovery of meaningful representations.

By linking supervision and sparsity within a unified geometric and statistical framework, this work establishes common ground between two interpretability communities. CBMs contribute *guidance* (anchoring interpretability in human-aligned structure) while SAEs contribute *scalability*, extending it to large, unlabeled models. Their synthesis imply that supervision can guide discovery, and discovery can refine supervision, advancing a unified, operational science of interpretable representation learning.

2. Concept Cones: A Unifying Geometry for Concept Learning

In this section we formalize a shared view of concept learning through the lens of dictionary learning. Our aim is to show that Concept Bottleneck Models (CBMs) and Sparse Autoencoders (SAEs) solve the same inverse problem under different regularization.

Notation. Let $\mathcal{X} \subset \mathbb{R}^{H \times W \times 3}$ be the input space and $\mathcal{A} \subset \mathbb{R}^d$ a feature space of a fixed representation map $\mathbf{f} : \mathcal{X} \rightarrow \mathcal{A}$. Given a dataset $\mathbf{X} = (\mathbf{x}_1, \dots, \mathbf{x}_n) \subset \mathcal{X}$, define the activation matrix $\mathbf{A} = \mathbf{f}(\mathbf{X}) \in \mathbb{R}^{n \times d}$ with rows $\mathbf{a}_i = \mathbf{f}(\mathbf{x}_i)^\top$. Let c denote the number of concepts, $\mathbf{D} \in \mathbb{R}^{c \times d}$ a concept dictionary (rows are atoms), and $\mathbf{Z} \in \mathbb{R}^{n \times c}$ a code matrix (rows are per-example concept coordinates).

Data-generating process. We assume observations arise from a latent space of compositional factors of variation. Let $\mathcal{C} \subset \mathbb{R}^K$ (here K is the dimension of the latent space, so the the number of independent attribute, e.g.: hair color, pose, lighting, expression, shapes, textures, etc.) be a latent

space with product measure $P_c = \bigotimes_{k=1}^K P_k$, where P_k is the probability distribution of the k -th latent factor the coordinate c_k . Let $\mathbf{G} : \mathcal{C} \rightarrow \mathcal{X}$ be a measurable map that is C^1 and injective on a full-measure subset of \mathcal{C} . The data distribution on \mathcal{X} is the pushforward $P_{\mathbf{x}} = \mathbf{G}_\# P_c$. When \mathbf{G} is a diffeomorphism onto its image and p_c is a density,

$$p_{\mathbf{x}}(\mathbf{x}) = p_c(\mathbf{G}^{-1}(\mathbf{x})) |\det \mathbf{J}_{\mathbf{G}^{-1}}(\mathbf{x})|. \quad (1)$$

Each coordinate c_k encodes a part or attribute that contributes to $\mathbf{x} = \mathbf{G}(\mathbf{c})$ through composition.

Definition 1 (Concept as inversion of latent factors). *A concept c_k is a coordinate of a measurable right-inverse $\mathbf{H} : \mathcal{A} \rightarrow \mathcal{C}$ of the data-to-feature map $\mathbf{f} \circ \mathbf{G}$. Formally, $\mathbf{H} \circ \mathbf{f} \circ \mathbf{G}(\mathbf{c}) \approx \mathbf{c}$ in expectation under P_c . Equivalently, the k -th concept is $\mathbf{H}_k(\mathbf{a})$, which estimates the latent factor c_k from an activation $\mathbf{a} \in \mathcal{A}$.*

With Definition 1 in hand, concept recovery is the problem of inverting the map $\mathbf{f} \circ \mathbf{G}$ on its image. Concretely, one seeks a measurable right-inverse $\mathbf{H} : \mathcal{A} \rightarrow \mathcal{C}$ so that $\mathbf{H} \circ \mathbf{f} \circ \mathbf{G} \approx \text{Id}_{\mathcal{C}}$ in expectation. Because \mathbf{f} is generally nonlinear and high dimensional, we work in a linear chart of \mathcal{A} and approximate inversion by learning a low-dimensional coordinate system for activations. This leads naturally to concept extraction as *dictionary learning* formulation [28, 56, 57] that we recall now.

Unsupervised Concept Extraction as Dictionary Learning. As shown by previous work, most of the unsupervised concept extraction method boils own to dictionary learning that seek to approximate the activation matrix $\mathbf{A} \in \mathbb{R}^{n \times d}$ via a factorization $\mathbf{A} \approx \mathbf{ZD}$, where $\mathbf{Z} \in \mathbb{R}^{n \times c}$ contains per-example codes (concepts) and $\mathbf{D} \in \mathbb{R}^{c \times d}$ is a dictionary whose rows represent concept directions (atoms). The different methods of unsupervised concept extraction that have been proposed *only differ in their constraints* :

$$(\mathbf{Z}^*, \mathbf{D}^*) = \arg \min_{\mathbf{Z}, \mathbf{D}} \|\mathbf{A} - \mathbf{ZD}\|_F^2, \text{ subject to} \quad (2)$$

$$\begin{cases} \forall i, \mathbf{Z}_i \in \{\mathbf{e}_1, \dots, \mathbf{e}_k\}, & (\text{ACE [34]}), \\ \mathbf{DD}^\top = \mathbf{I}, & (\text{ICE [38, 106]}), \\ \mathbf{Z} \geq 0, \mathbf{D} \geq 0, & (\text{CRAFT [29]}), \\ \mathbf{D}_i \in \text{conv}(\mathbf{A}) & (\text{Archetypal Analysis [30, 101]}), \\ \mathbf{Z} = \Psi_\theta(\mathbf{A}), \|\mathbf{Z}\|_0 \leq K, & (\text{SAEs [9, 37, 49, 75, 87]}) \end{cases}$$

where $\Psi(\cdot)$ is generally a linear encoder equipped with a ReLU activation and a sparsity projection (such as TopK [32], BatchTopK [10], or JumpReLU [45]). Across all these formulations, the learned codes \mathbf{Z} are nonnegative or zero, meaning that activations are reconstructed through additive, parts-based combinations of concept directions.

Supervised Concept Extraction with Linear Bottlenecks. Having cast unsupervised methods as dictionary learning, we now show that Concept Bottleneck Models (CBMs) also fit a regular template that we should clarify now. Essentially, it add supervision on the codes to align them with labeled concepts. For activations $\mathbf{a}_i \in \mathcal{A}$, a CBM predicts concept scores \hat{c}_i and labels $\hat{\mathbf{y}}_i$ through a linear bottleneck. Most CBM variants seek to learn a dictionary $\mathbf{W}_c \in \mathbb{R}^{c \times d}$ whose rows represent concept directions and codes (concept coefficient) $\hat{c}_i \in [0, 1]^c$ that are predicted from activations via $\hat{c}_i = \sigma(\mathbf{a}_i \mathbf{W}_c^\top + \mathbf{b}_c)$, followed by a linear classifier $\hat{\mathbf{y}}_i = \text{softmax}(\hat{c}_i \mathbf{W}_y^\top + \mathbf{b}_y)$. The different CBM architectures that have been proposed *only differ in their supervision and training*:

$$(\mathbf{W}_c^*, \mathbf{W}_y^*) = \arg \min_{\mathbf{W}_c, \mathbf{W}_y} \sum_{i=1}^n \mathcal{L}_{\text{CE}}(\hat{\mathbf{y}}_i, \mathbf{y}_i) + \lambda \mathcal{L}_{\text{BCE}}(\hat{c}_i, c_i),$$

subject to

$$\begin{cases} \lambda > 0, \text{ joint training,} & (\text{Joint CBM [59]}), \\ \lambda > 0, \text{ sequential training,} & (\text{Sequential CBM [59, 92]}), \\ \lambda = 0, \mathbf{W}_c = \mathbf{D}_{\text{LLM}}, & (\text{Label-Free CBM [71]}), \\ \lambda = 0, \mathbf{W}_c = \mathbf{D}_{\text{Bank}}, & (\text{Post-hoc CBM [8, 102]}), \\ \lambda = 0, \mathbf{W}_c = \mathbf{D}_{\text{SAE}}, & (\text{DN CBM [81]}), \\ \hat{c}_i \sim \mathcal{N}(\sigma(\mu(\mathbf{a}_i)), \Sigma(\mathbf{a}_i)), & (\text{Stochastic CBM [98]}), \\ \lambda = 0, \mathbf{W}_c = \mathbf{D}_{\text{CLIP}}, & (\text{Clip-QDA [52]}). \end{cases} \quad (3)$$

Here \mathbf{D}_{LLM} denotes concepts generated by large language models (e.g., GPT-3) and embedded via CLIP, \mathbf{D}_{Bank} represents predefined concept banks or post-hoc extracted directions (e.g., via *Broden* dataset), \mathbf{D}_{SAE} refers to dictionary atoms learned by SAEs, and \mathbf{D}_{CLIP} denotes principal components of CLIP text embeddings. Note that some methods introduce architectural variations: Post-hoc CBM may include residual connections, CLIP-QDA uses quadratic discriminant analysis instead of linear classification, and Stochastic CBM samples concept activations from learned distributions. Independent, sequential, and joint training regimes correspond to different optimization schedules on the same objective, thus preserving the bottleneck geometry. For detailed descriptions of each variant, see Appendix A.

Now that we have studied the two different frameworks of unsupervised and supervised concept extraction, a natural question arises: *what structure unifies these seemingly distinct approaches?* We now show that a possible answer is a specific geometric structure that we will now describe.

Concept Cones: A Unifying Geometric Framework. A key observation unifying supervised and unsupervised approaches is that the activation function of the CBM ensures all concept codes (coefficients) satisfy $c \geq 0$, exactly as in unsupervised dictionary learning where codes are con-

strained to be nonnegative (Equation 2). Thus both supervised methods (CBMs) and unsupervised methods (SAEs, CRAFT, etc.) produce *nonnegative codes* and learn a dictionary whose rows encode concept directions— \mathbf{W}_c for CBMs and \mathbf{D} for unsupervised extractors. The geometric consequence is that the representable activation subspace is characterized by the *conic hull* generated by these concept directions. This conical structure provides a unified view of concept extraction across approaches.

Definition 2 (Concept Cone). *Given a concept dictionary $\mathbf{D} \in \mathbb{R}^{c \times d}$ (equivalently \mathbf{W}_c for CBMs), we define the associated concept cone as*

$$\begin{aligned} \mathcal{C}_{\mathbf{D}} &= \{ \mathbf{v} \in \mathbb{R}^d : \mathbf{v} = \boldsymbol{\alpha}^\top \mathbf{D} \text{ for some } \boldsymbol{\alpha} \in \mathbb{R}_+^c \} \\ &= \text{cone}(\mathbf{D}_1, \dots, \mathbf{D}_c), \end{aligned} \quad (4)$$

where $\mathbf{D}_i \in \mathbb{R}^d$ denotes the i -th row (concept direction) of \mathbf{D} , and $\text{cone}(\cdot)$ denotes the conic hull.

This geometric perspective yields several important insights formalized in the following observation.

Observation 1 (Concept Cones Unify Extraction Methods). *Let $\mathbf{D} \in \mathbb{R}^{c \times d}$ be a concept dictionary learned by any method in Equation (2) or Equation (3). Then:*

- (i) **Projection operator:** Both supervised and unsupervised methods implicitly learn a projection operator $\Pi_{\mathcal{C}_{\mathbf{D}}} : \mathbb{R}^d \rightarrow \mathcal{C}_{\mathbf{D}}$ that maps activations onto the concept cone via $\Pi_{\mathcal{C}_{\mathbf{D}}}(\mathbf{a}) = \hat{\mathbf{c}}^\top \mathbf{D}$ where $\hat{\mathbf{c}} \geq 0$.
- (ii) **Shared geometric structure:** Supervised methods (CBMs) and unsupervised methods optimize for different objectives – task performance vs. reconstruction – but both search for a convex cone $\mathcal{C}_{\mathbf{D}}$ in activation space that captures the relevant subspace of \mathcal{A} .
- (iii) **Concept recoverability:** A concept direction $\mathbf{v} \in \mathbb{R}^d$ learned by one method is recoverable from dictionary \mathbf{D} learned by another if and only if $\mathbf{v} \in \mathcal{C}_{\mathbf{D}}$, i.e., there exists $\boldsymbol{\alpha} \in \mathbb{R}_+^c$ such that $\mathbf{v} = \boldsymbol{\alpha}^\top \mathbf{D}$. Agreement between methods is thus quantified by their cone overlap.

See details in Appendix B. This geometric unification motivates our approach: rather than treating supervised and unsupervised concept extraction as separate paradigms, we view them as alternative procedures for selecting a concept cone in activation space and we clarify how CBM can actually guide unsupervised concept research: by giving some desirable concept cone that an SAE should recover. In the next section, we operationalize this perspective by introducing metrics to quantify cone overlap and studying empirically how CBM and SAE cones align.

2.1. Operationalization of Cone Overlap

The geometric framework established in Proposition 1 clarifies the relationship between supervised and unsupervised

concept extraction, but also raises a natural question: *do SAEs actually discover plausible concepts [47], as encoded by CBMs?* We do not expect perfect alignment – SAEs discover a broad spectrum of concepts to reconstruct activations, while CBMs focus on a small set of task-relevant, human-desirable (or at minimum plausible [47]) concepts. However, our assumption is that the SAE concept cone $\mathcal{C}_{\mathbf{D}_{\text{SAE}}}$ should *contain* or closely approximate the CBM concept cone $\mathcal{C}_{\mathbf{W}_c}$. More precisely, we expect that a *sparse subset* of SAE concepts can recover CBM concepts through nonnegative combinations. Thanks to the cone geometry, we can now formalize this intuition and derive concrete metrics to measure it. Before formally introduce our metrics, we propose to clarify exactly the role that CBM can play and why they matter for unsupervised concepts extraction research.

Why CBM Concepts Matter for SAE Evaluation. A critical challenge in SAE research is the absence of ground truth for what constitutes a "correct" concept decomposition. Recall from Definition 1 that a concept c_k is formally a coordinate of a measurable right-inverse $\mathbf{H} : \mathcal{A} \rightarrow \mathcal{C}$ recovering latent factors \mathbf{c} from activations \mathbf{a} . However, this inverse is generally non-unique [58, 63]: many factorizations \mathbf{H} can approximately satisfy $\mathbf{H} \circ \mathbf{f} \circ \mathbf{G}(\mathbf{c}) \approx \mathbf{c}$, and without access to the true data generating process \mathbf{G} or latent factors \mathbf{c} , we cannot determine which is "correct." This theoretical ambiguity manifests empirically: minor changes in hyperparameters (sparsity penalty, dictionary size, initialization) yield drastically different learned dictionaries \mathbf{D}_{SAE} , all achieving similar reconstruction error [30, 78]. Recent work has proliferated diverse SAE variants – standard SAEs [9], TopK [32], JumpReLU [80], Transcoders [40], Matching-Pursuit [16] – yet without ground truth, evaluation relies on proxy metrics (reconstruction loss, sparsity, task performance) that do not directly measure concept plausibility. This is where CBMs provide crucial value: they encode a human-curated basis of concepts deemed plausible [47] and desirable through explicit supervision or expert knowledge. While CBM concepts are not ground truth (they reflect human choices, biases, and annotation limitations) they are a first order approximation of the kind of structure we seek SAEs to discover. The concept cone framework (Definition 2) operationalizes this intuition: we can quantify how well an SAE cone $\mathcal{C}_{\mathbf{D}_{\text{SAE}}}$ aligns with a CBM cone $\mathcal{C}_{\mathbf{W}_c}$ through concrete metrics. This alignment does not constitute ground truth validation but rather a *desirability signal*: an SAE that recovers human-annotated concepts through sparse, nonnegative combinations provides evidence of latching onto plausible structure, making its decompositions more likely to be meaningful, useful, and actionable. Moreover, by comparing multiple SAE variants on their ability to recover the same CBM concepts, we can assess which inductive biases (sparsity mechanisms, expansion factors, architectures) sys-

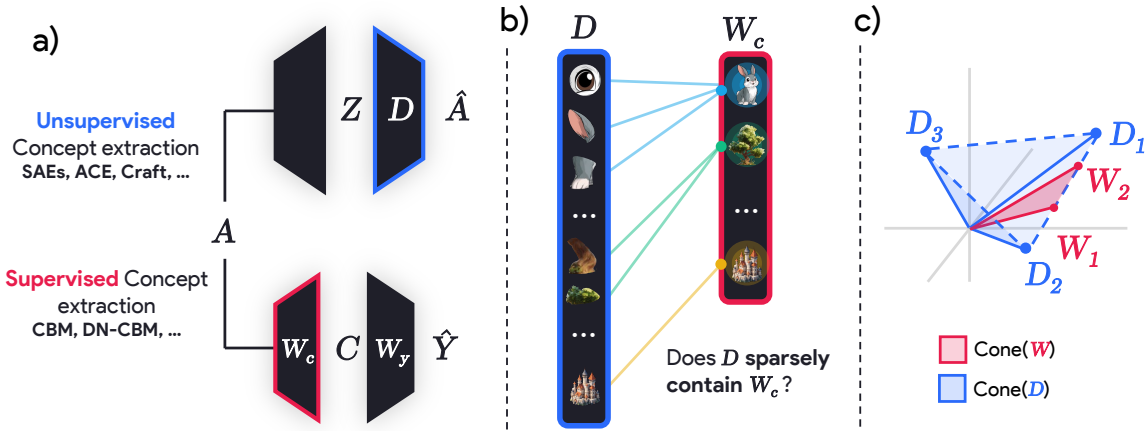


Figure 2. **CBMs as anchors for unsupervised concept discovery.** Both supervised and unsupervised methods learn linear directions in activation space \mathcal{A} , but they do so under different objectives. Unsupervised approaches such as SAEs decompose activations A into a dictionary D and sparse codes Z , uncovering emergent concept directions without human supervision. CBMs, in contrast, learn a set of concept directions W_c aligned with annotated or language-derived concepts that are known to be meaningful to humans. This contrast raises a central question: *do the directions discovered by an SAE contain, or at least sparsely approximate, the human-desirable directions encoded by a CBM?* Geometrically, this amounts to testing whether the supervised concept cone $\mathcal{C}_{W_c} = \{W_c^\top \beta : \beta \geq 0\}$ is included in the unsupervised cone $\mathcal{C}_D = \{D^\top \alpha : \alpha \geq 0\}$. If so, the SAE has discovered a basis rich enough to represent human-aligned semantics through simple nonnegative combinations of its atoms. This viewpoint reframes CBMs not as competitors to SAEs but as geometric reference systems: they define desirable regions of concept space whose containment within the SAE cone quantifies the extent to which unsupervised discovery find plausible [47] concepts.

tematically yield more plausible decompositions, providing actionable design insights.

Formalizing the Containment Hypothesis. Having established our central hypothesis : CBMs provide human-desirable concept directions that can serve as anchors for evaluating or guiding SAEs; while recognizing their limitation as human-constructed rather than ground-truth factors, we now turn to a formal statement of this idea.

The *containment hypothesis* asserts that if an unsupervised dictionary faithfully captures the meaningful structure of the representation space, then the concept directions learned by a CBM should be contained within, or well-approximated by, the cone spanned by the unsupervised atoms. In the following, we translate this hypothesis into measurable quantities that express how much of the CBM concept space is recoverable from an SAE dictionary. Formally, for a CBM concept direction $v_i \in \mathbb{R}^d$ (the i -th row of W_c), we seek nonnegative coefficients $\alpha_i \in \mathbb{R}_+^{\text{CSAE}}$ such that $v_i \approx \alpha_i^\top D_{\text{SAE}}$. By Proposition 1(iii), this is equivalent to asking whether $v_i \in \mathcal{C}_{D_{\text{SAE}}}$ or lies close to it. Crucially, we further hypothesize that this recovery should be *sparse*: only a small number of SAE concepts should be needed to reconstruct each CBM concept, reflecting the compositional structure of human-interpretable notions. This leads us to formulate the following sparse nonnegative reconstruction problem for each CBM concept:

$$\alpha_i^* = \arg \min_{\alpha \geq 0} \|v_i - \alpha^\top D_{\text{SAE}}\|_2^2 + \lambda \|\alpha\|_1 \quad (5)$$

where $\lambda > 0$ controls sparsity. The reconstruction error $\|v_i - \alpha_i^{*\top} D_{\text{SAE}}\|_2$ measures how well the CBM concept

lies in (or near) the SAE cone, while the sparsity $\|\alpha_i^*\|_0$ quantifies the complexity of the representation.

Metrics The cone formalism provides a geometric bridge between supervised and unsupervised concept learning. To assess how closely the unsupervised concept cone $\mathcal{C}_{D_{\text{SAE}}}$ aligns with the supervised concept cone \mathcal{C}_{W_c} , we introduce a set of complementary quantitative measures that capture containment, geometric alignment, and activation-level correspondence. Together, these metrics turn the qualitative notion of “concept alignment” into a concrete and measurable relation between CBMs and SAEs.

Geometric Alignment. The first family of metrics evaluates whether the concept directions identified by a CBM lie within, or close to, the cone spanned by the SAE dictionary. Given the sparse reconstruction problem in Equation 5, we can measure for each CBM direction v_i a normalized residual

$$\delta_i = \frac{\|v_i - \alpha_i^{*\top} D_{\text{SAE}}\|_2}{\|v_i\|_2}, \quad (6)$$

which expresses the distance of v_i to the SAE cone. A small reconstruction error $\delta_i \approx 0$ indicates that the CBM concept is representable as a nonnegative combination of SAE atoms. The average reconstruction error $\bar{\delta}$ over all concepts thus provides a measure of local containment between the two cones. In addition to accuracy, we also examine the **sparsity of recovery** by counting the number of active coefficients in the optimal reconstruction, $s_i = \|\alpha_i^*\|_0 = |\{j : \alpha_{ij}^* > 0\}|$. A low sparsity value indicates that CBM concepts correspond to simple, compositional mixtures of SAE atoms rather than diffuse or entangled combinations. Finally, a global measure

of containment can be obtained through the **cone coverage**, defined as

$$\text{Cov} = \frac{\sum_i \|\alpha_i^{*\top} \mathbf{D}_{\text{SAE}}\|_2^2}{\sum_i \|\mathbf{v}_i\|_2^2}. \quad (7)$$

A coverage close to one means that the unsupervised cone nearly subsumes the CBM cone, while lower values signal that important semantic directions fall outside the space spanned by the SAE.

Containment ensures inclusion but not necessarily directional agreement. To evaluate whether both models discover similarly oriented concept axes, we compare the directions that generate each cone. The rows of \mathbf{D}_{SAE} and \mathbf{W}_c define two sets of vectors in the same activation space. Their geometric alignment is captured by the average maximal correlation

$$\rho_{\text{geom}} = \frac{1}{c_{\text{SAE}}} \sum_j \max_i |\text{corr}(\mathbf{d}_j, \mathbf{w}_i)|, \quad (8)$$

which quantifies how well each SAE atom aligns with some CBM direction. High values of ρ_{geom} imply that the geometric axes of both models are closely aligned, suggesting that the SAE has recovered the orientation of human-defined concepts.

Statistical Alignment. The final family of metrics compares the behavior of both models across data samples rather than in parameter space. Each model defines a code matrix of activations, $\mathbf{Z}_{\ell}^{\text{SAE}}$ and $\mathbf{Z}_{\ell}^{\text{CBM}}$, whose columns describe the activity of individual concepts or atoms over the dataset. By correlating these columns, we obtain a measure of statistical correspondence between their respective concept activations. For each SAE activation $\mathbf{Z}_{\cdot j}^{\text{SAE}}$, we compute the maximal correlation with any CBM activation $\mathbf{Z}_{\cdot i}^{\text{CBM}}$ and average these maxima across all j to obtain

$$\rho_{\text{act}} = \frac{1}{c_{\text{SAE}}} \sum_j \max_i |\text{corr}(\mathbf{Z}_{\cdot j}^{\text{SAE}}, \mathbf{Z}_{\cdot i}^{\text{CBM}})|. \quad (9)$$

High values of ρ_{act} indicate that both models activate in similar ways on the same inputs, capturing comparable semantic dimensions even if their parameterizations differ. A more global view is given by a simple **regression predictability** analysis, in which we fit a linear regression mapping the SAE activations to those of the CBM, $\hat{\mathbf{Z}}_{\ell}^{\text{CBM}} = \Phi(\mathbf{Z}_{\ell}^{\text{SAE}})$, and compute the coefficient of determination

$$R^2 = 1 - \frac{\sum_i \|\mathbf{Z}_{\ell, i}^{\text{CBM}} - \hat{\mathbf{Z}}_{\ell, i}^{\text{CBM}}\|_2^2}{\sum_i \|\mathbf{Z}_{\ell, i}^{\text{CBM}} - \bar{\mathbf{Z}}_{\ell}^{\text{CBM}}\|_2^2}. \quad (10)$$

A high R^2 score indicates that the SAE’s representation is predictive of the CBM’s concept space, reinforcing the idea that both encode similar semantic structure in their activations.

We introduce two complementary metrics to further characterize the statistical alignment between the SAE and CBM representations. First, to assess how *distributed* or *concentrated* the SAE–CBM correspondence is, we compute the empirical frequency of SAE-to-CBM matches:

$$p_i = \frac{1}{c_{\text{SAE}}} |\{j : m(j) = i\}|, m(j) = \arg \max_i |\text{corr}(\mathbf{Z}_{\cdot j}^{\text{SAE}}, \mathbf{Z}_{\cdot i}^{\text{CBM}})|.$$

We then define the normalized Shannon entropy:

$$H_{\text{match}} = -\frac{1}{\log(c_{\text{CBM}})} \sum_{i=1}^{c_{\text{CBM}}} p_i \log p_i. \quad (11)$$

A low value of H_{match} indicates that most SAE concepts align with only a few CBM concepts (*concentrated mapping*), while a high value reflects a more uniform alignment (*distributed mapping*), suggesting that SAE concepts capture diverse semantic patterns spanning multiple CBM-defined concepts.

Second, to measure the agreement between models at the data-sample level, we compare the top- k active concepts in both representations. For each sample t , we extract: $\mathcal{T}_t^{\text{CBM}} = \text{Top-}k(\mathbf{Z}_{t, \cdot}^{\text{CBM}})$, $\mathcal{T}_t^{\text{SAE}} = \text{Top-}k(\mathbf{Z}_{t, \cdot}^{\text{SAE}})$, where $\text{Top-}k(v)$ returns the indices of the k largest entries of v . We then map SAE indices to CBM concepts using the correspondence $m(\cdot)$:

$$\hat{\mathcal{T}}_t^{\text{SAE} \rightarrow \text{CBM}} = \{m(j) : j \in \mathcal{T}_t^{\text{SAE}}\}. \quad (12)$$

Finally, we compute the precision, recall, and F1 scores between $\hat{\mathcal{T}}_t^{\text{SAE} \rightarrow \text{CBM}}$ and $\mathcal{T}_t^{\text{CBM}}$, quantifying how well the SAE’s most active concepts, when mapped into CBM space, recover the ground-truth concepts identified by the CBM.

Discussion. These three metrics provide complementary views of concepts overlap. The reconstruction error, sparsity, and coverage quantify the *containment* of one cone within another; the geometric and activation correlations measure the *alignment* of their axes and activations; and the regression predictability provides a coarse but global estimate of how information transfers between the two spaces. All quantities are efficiently computable: sparse recovery reduces to standard Lasso regression [96], and correlation or regression metrics scale linearly with the number of concepts. These measures thus make the abstract notion of cone alignment empirically tractable, providing a principled way to compare supervised and unsupervised concept representations within a unified geometric framework.

3. Experiments

Experimental Settings. We train three vision backbones: ResNet-50[42], ViT[23], and DINov2[72]. All networks are trained on ImageNet[83], and also on CUB[100]. On top of these backbones, we train six families of SAEs: Vanilla, TopK[32], BatchTopK[10], Jump[80], MP[16], and

Archetypal[30]. Unless otherwise stated, the expansion factor and sparsity parameters are chosen following standard SAE practice, namely the expansion factor is equal to $\times 2$ and the sparsity parameters are equal to 0.005. The CBM construction and detailed settings are given in Appendix C.

We conduct several complementary analyses: *(i)* a sanity-check experiment validating the behavior of the metrics under controlled conditions; *(ii)* a study of how SAE variants affect geometric and statistical alignment; *(iii)* an analysis of the effects of expansion factors and sparsity constraints; *(iv)* a layer-wise exploration to study the influence of depth.

Sanity Check Experiment. The objective of this experiment is to verify that the proposed metrics behave consistently across two controlled conditions: a TopK SAE trained on the correct dataset, and a TopK SAE that is untrained (randomly initialized). This configuration enables us to evaluate whether the metrics reflect meaningful alignment or merely respond to superficial activation patterns, addressing recent claims that randomly initialized SAEs can achieve comparable auto-interpretability scores [44]. The results of this experiment are presented in Table 1. As anticipated, the trained SAE exhibits mainly higher geometric and statistical alignment with the CBM, while the random SAE yields weaker alignment scores, with the exception of Coverage, which tends to be artificially inflated in the absence of learned structure. The decrease in correlation and R^2 values for the random model confirms that its activations are less predictive of the CBM and therefore capture fewer semantically coherent patterns according to our plausibility framework. This finding contests claims that untrained SAEs produce interpretable features: while random directions may admit post-hoc linguistic labels [44], our cone-based metrics reveal they fail to recover human-defined concept geometries. Conversely, the trained SAE leads to stronger alignment across metrics, validating that the metrics are sensitive to training quality and capture the emergence of plausible conceptual structure during learning. Overall, this sanity check demonstrates that the proposed evaluation framework successfully distinguishes meaningful learned representations from random activation structures, providing evidence that training does produce more human-aligned concept decompositions.

BatchTopK and Archetypal SAEs Show Superior Alignment. We compare the SAE variants across CUB and ImageNet using ResNet-50, ViT, and DINOv2 backbones. Results appear in Table 2, with configurations matched to comparable sparsity levels where feasible. All variants achieve high R^2 values, indicating substantial predictive alignment with CBM representations. However, BatchTopK and Archetypal consistently exhibit superior coverage alongside competitive geometric alignment, suggesting their regularization schemes facilitate discovery of

Table 1. Sanity check results for ResNet-50 ViT and Dino models trained on CUB and ImageNet (IN), and TopK SAEs trained either on CUB, ImageNet, as well as an untrained SAE. Each SAE is evaluated on both the CUB and ImageNet (IN) datasets.

	(Test dataset/train dataset)	ρ_{geom}	ρ_{act}	Cov	R^2	H_{match}	F1
R50	CUB / CUB	0.099	0.062	0.241	0.968	6.89	0.224
	CUB / NONE	0.063	0.052	0.662	0.864	4.86	0.235
	IN / IN	0.156	0.086	0.193	0.881	6.71	0.052
	IN / NONE	0.068	0.052	0.869	0.729	8.21	0.074
ViT	CUB / CUB	0.208	0.066	0.261	0.736	6.95	0.170
	CUB / NONE	0.103	0.075	0.666	0.638	6.82	0.168
	IN / IN	0.116	0.145	0.012	0.491	6.27	0.061
	IN / NONE	0.070	0.047	0.908	0.173	6.59	0.053
Dino V2	CUB / CUB	0.331	0.076	0.275	0.847	6.71	0.170
	CUB / NONE	0.102	0.096	0.736	0.795	6.78	0.166
	IN / IN	0.114	0.119	0.028	0.409	5.44	0.060
	IN / NONE	0.078	0.048	0.745	0.268	6.34	0.068

broader concept repertoires without sacrificing directional correspondence. While no method dominates uniformly across all metrics, these results indicate that sparsity mechanism constitutes a consequential architectural choice shaping both the geometry and plausibility of learned concept spaces.

Table 2. Comparison of different SAE variants on CUB using a ResNet-50 (R50), ViT and Dino V2. Metrics assess geometric and activation alignment.

Dataset-Backbone	SAE Type	Sparsity	ρ_{geom}	ρ_{act}	Cov	R^2	H_{match}	Prec.	Rec.	F1
CUB-R50	Vanilla	0.985	0.101	0.088	0.350	0.968	6.55	0.199	0.280	0.230
	TopK	0.995	0.099	0.062	0.241	0.968	6.89	0.182	0.297	0.224
	BatchTopK	0.988	0.098	0.075	0.657	0.973	5.77	0.231	0.366	0.282
	Jump	0.980	0.098	0.095	0.419	0.974	6.34	0.197	0.285	0.230
	MP	0.988	0.100	0.088	0.363	0.968	6.51	0.185	0.264	0.215
	Archetypal	0.991	0.100	0.082	0.350	0.967	6.07	0.207	0.330	0.253
CUB-ViT	Vanilla	0.990	0.127	0.099	0.152	0.752	6.86	0.108	0.166	0.130
	TopK	0.995	0.208	0.066	0.260	0.736	6.95	0.133	0.237	0.170
	Jump	0.967	0.118	0.137	0.362	0.807	6.59	0.150	0.235	0.182
	BatchTopK	0.969	0.114	0.089	0.607	0.768	5.03	0.159	0.276	0.201
	MP	0.997	0.129	0.071	0.133	0.778	6.37	0.062	0.115	0.081
	Archetypal	0.974	0.115	0.092	0.230	0.797	5.655	0.174	0.294	0.217
CUB-Dino	Vanilla	0.963	0.134	0.153	0.676	0.928	6.79	0.226	0.281	0.245
	TopK	0.995	0.331	0.076	0.275	0.848	6.71	0.137	0.228	0.170
	Jump	0.949	0.131	0.156	0.706	0.938	6.81	0.242	0.323	0.272
	BatchTopK	0.982	0.127	0.077	0.632	0.835	5.47	0.150	0.267	0.191
	MP	0.997	0.174	0.053	0.193	0.870	4.13	0.138	0.235	0.135
	Archetypal	0.994	0.132	0.079	0.395	0.893	6.85	0.144	0.221	0.172

A Sparsity Sweet Spot. We systematically vary sparsity in TopK SAEs via the target ℓ_0 parameter, which controls the proportion of active units per sample. Results across CUB and ImageNet with multiple backbones (Appendix D.1, Figure 3(a)) reveal a consistent pattern: as sparsity decreases—permitting more active dictionary atoms—coverage, R^2 , and sample-level F1 improve substantially, indicating that denser codes better reconstruct the CBM concept space. Geometric alignment (ρ_{geom}), however, exhibits the opposite trend, declining as representations become less concentrated. This inverse relationship suggests a potential tension: aggressive sparsity produces plausible, localized prototypes at the expense of completeness, while relaxed sparsity enhances concept recovery but disperses structure across more atoms. Empirically, intermediate sparsity regimes ($\approx 0.01\text{--}0.05\%$ of sparsity) achieve favorable balance, maintaining reasonable geometric fidelity while attaining high coverage. Once again, these findings indicate

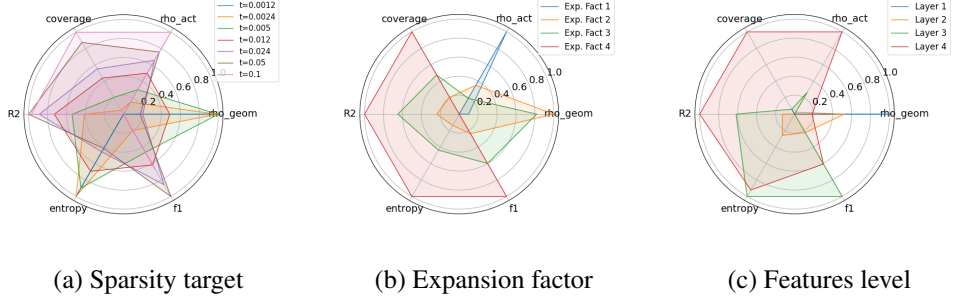


Figure 3. Radar plot illustrating the influence of the (a) **sparsity target**, (b) **expansion factor**, and (c) **features level** on TopK Sparse Autoencoder (SAE) performance for both CUB and ImageNet datasets. Each axis corresponds to a normalized metric.

that sparsity is a substantive design parameter governing the plausibility of the found dictionary.

Expansion Factor Sweet Spot. We examine the influence of latent expansion factor (the ratio of dictionary size to input dimensionality) on TopK SAE performance. Increasing this factor enlarges representational capacity, permitting the model to discover more distinct concept directions. Results across CUB and ImageNet (Appendix D.3, Figure 3(b)) demonstrate that larger latent spaces systematically improve coverage, R^2 , and sample-level F1, though geometric alignment (ρ_{geom}) and activation correlation (ρ_{act}) decline modestly as representations distribute across more atoms. A sweet spot emerges at approximately $3 \times$ expansion. Beyond this threshold, further expansion yields diminishing returns: coverage saturates while directional alignment continues to diffuse. These findings suggest that expansion factor, like sparsity, governs a tradeoff between expressive capacity and interpretive concentration, with intermediate regimes offering the most favorable balance for recovering plausible concepts.

Layer-wise evaluation of TopK SAEs. We investigate how the semantic alignment between the SAE and the CBM evolves across different stages of the ResNet-50 backbone. Specifically, we extract features *after the pooling operation of each residual block* (i.e., after the spatial average pooling of stages 1–4) and train a separate TopK SAE on each set of features. This setup allows us to assess at which depth the backbone’s representation best matches the CBM concept space. As shown in Appendix D.2 and Figure 3(c), lower stages (Layers 1–2) capture mostly low-level visual attributes such as edges, colors, and textures, while deeper stages (Layers 3–4) encode increasingly abstract and semantically structured information. Results reveal a clear depth-dependent trend. On CUB, deeper layers (particularly Layers 3 and 4) yield the strongest alignment, as indicated by higher R^2 , coverage, and F1 values. Layer 4 achieves the best predictability ($R^2 \approx 0.97$) and strong concept coverage,

while Layer 3 slightly surpasses it in F1 score. Conversely, earlier layers, despite showing higher geometric correlation, primarily represent local patterns that do not align with the CBM’s semantic dimensions. For ImageNet, the same tendency holds. Layers 3 and 4 again achieve the highest R^2 and coverage, confirming that post-pooling representations in the later blocks of ResNet-50 encode higher-level, concept-like features consistent with CBM semantics.

4. Conclusion

This work bridges two major paradigms in interpretability research namely CBMs and SAEs; by framing them as complementary instances of a shared dictionary-learning principle. Through this lens, we show that supervision and sparsity represent two distinct yet compatible forms of regularization that structure the same conceptual space: the former enforces human-aligned semantics, while the latter uncovers emergent statistical organization. Our experiments reveal that intermediate layers of pretrained backbones, particularly those following block-level pooling in ResNet architectures, exhibit the strongest semantic alignment with concept-level representations. Moderate sparsity and expanded latent capacity enable SAEs to uncover structured, interpretable concept dictionaries that parallel CBM-defined semantic dimensions. Together, these findings demonstrate that interpretability can emerge from the interplay between supervision and sparsity, offering both control and scalability. By establishing a unified framework for evaluating semantic alignment across supervised and unsupervised settings, this work provides a foundation for a more systematic, operational understanding of how deep networks internalize human-interpretable structure. Ultimately, our results suggest that the path toward truly interpretable foundation models lies not in choosing between supervision or discovery, but in harmonizing the two within a common geometric and statistical framework.

Acknowledgments: The authors thank Demba Ba for many fruitful discussions. This work was granted access to the HPC resources of IDRIS under the allocation 2024-AD011011970R4. This work has been made possible in part by a gift from the Chan Zuckerberg Initiative Foundation to establish the Kempner Institute for the Study of Natural and Artificial Intelligence at Harvard University. T.F. is supported by the Kempner Institute Research Fellowship.

References

- [1] Lucian Alecu, Hugues Bonnin, Thomas Fel, Laurent Gardes, Sébastien Gerchinovitz, Ludovic Ponsolle, Franck Mamalet, Éric Jenn, Vincent Mussot, Cyril Cappi, et al. Can we reconcile safety objectives with machine learning performances? *ERTS*, 2022.
- [2] Danis Alukaev, Semen Kiselev, Ilya Pershin, Bulat Ibragimov, Vladimir Ivanov, Alexey Kornaev, and Ivan Titov. Cross-modal conceptualization in bottleneck models. *Proceedings of the Conference on Empirical Methods in Natural Language Processing (EMNLP)*, 2023.
- [3] Sanjeev Arora, Yuanzhi Li, Yingyu Liang, Tengyu Ma, and Andrej Risteski. Linear algebraic structure of word senses, with applications to polysemy. *Transactions of the Association for Computational Linguistics*, 2018.
- [4] Sebastian Bach, Alexander Binder, Grégoire Montavon, Frederick Klauschen, Klaus-Robert Müller, and Wojciech Samek. On pixel-wise explanations for non-linear classifier decisions by layer-wise relevance propagation. *Public Library of Science (PloS One)*, 2015.
- [5] Federico Baldassarre, Marc Szafraniec, Basile Terver, Vasil Khalidov, Francisco Massa, Yann LeCun, Patrick Labatut, Maximilian Seitzer, and Piotr Bojanowski. Back to the features: Dino as a foundation for video world models. *ArXiv e-print*, 2025.
- [6] Randall Balestrieri, Jerome Pesenti, and Yann LeCun. Learning in high dimension always amounts to extrapolation. *ArXiv e-print*, 2021.
- [7] David Bau, Bolei Zhou, Aditya Khosla, Aude Oliva, and Antonio Torralba. Network dissection: Quantifying interpretability of deep visual representations. *Proceedings of the IEEE Conference on Computer Vision and Pattern Recognition (CVPR)*, 2017.
- [8] Usha Bhalla, Alex Oesterling, Suraj Srinivas, Flavio P Calmon, and Himabindu Lakkaraju. Interpreting clip with sparse linear concept embeddings (splice). *ArXiv e-print*, 2024.
- [9] Trenton Bricken, Adly Templeton, Joshua Batson, Brian Chen, Adam Jermyn, Tom Conerly, Nick Turner, Cem Anil, Carson Denison, Amanda Askell, Robert Lasenby, Yifan Wu, Shauna Kravec, Nicholas Schiefer, Tim Maxwell, Nicholas Joseph, Zac Hatfield-Dodds, Alex Tamkin, Karina Nguyen, Brayden McLean, Josiah E Burke, Tristan Hume, Shan Carter, Tom Henighan, and Christopher Olah. Towards monosemanticity: Decomposing language models with dictionary learning. *Transformer Circuits Thread*, 2023.
- [10] Bart Bussmann, Patrick Leask, and Neel Nanda. Batchtopk sparse autoencoders. *ArXiv e-print*, 2024.
- [11] Kushal Chauhan, Rishabh Tiwari, Jan Freyberg, Pradeep Shenoy, and Krishnamurthy Dvijotham. Interactive concept bottleneck models. *Proceedings of the AAAI Conference on Artificial Intelligence (AAAI)*, 2023.
- [12] Sofia Chorna, Kateryna Tarelkina, Eloise Berthier, and Gianni Franchi. Concept-based mechanistic interpretability using structured knowledge graphs. *arXiv preprint arXiv:2507.05810*, 2025.
- [13] SueYeon Chung. Neural population geometry: An approach for understanding biological and artificial neural networks. *Current opinion in neurobiology*, 2021.
- [14] Uri Cohen, SueYeon Chung, Daniel D Lee, and Haim Sompolinsky. Separability and geometry of object manifolds in deep neural networks. *Nature communications*, 2020.
- [15] Julien Colin, Thomas Fel, Rémi Cadène, and Thomas Serre. What i cannot predict, i do not understand: A human-centered evaluation framework for explainability methods. *Advances in Neural Information Processing Systems (NeurIPS)*, 2021.
- [16] Valérie Costa, Thomas Fel, Ekdeep Singh Lubana, Bahareh Tolooshams, and Demba Ba. From flat to hierarchical: Extracting sparse representations with matching pursuit. *Advances in Neural Information Processing Systems (NeurIPS)*, 2025.
- [17] Hoagy Cunningham, Aidan Ewart, Logan Riggs, Robert Huben, and Lee Sharkey. Sparse autoencoders find highly interpretable features in language models. *ArXiv e-print*, 2023.
- [18] Timothée Darcet, Maxime Oquab, Julien Mairal, and Piotr Bojanowski. Vision transformers need registers. *ArXiv e-print*, 2023.
- [19] Nicola Debole, Pietro Barbiero, Francesco Giannini, Andrea Passerini, Stefano Tesso, and Emanuele Marconato. If concept bottlenecks are the question, are foundation models the answer? *arXiv preprint arXiv:2504.19774*, 2025.
- [20] Mostafa Dehghani, Josip Djolonga, Basil Mustafa, Piotr Padlewski, Jonathan Heek, Justin Gilmer, Andreas Peter Steiner, Mathilde Caron, Robert Geirhos, Ibrahim Alabdulmohsin, et al. Scaling vision transformers to 22 billion parameters. *Proceedings of the International Conference on Machine Learning (ICML)*, 2023.
- [21] Natalia Díaz-Rodríguez, Alberto Lamas, Jules Sanchez, Gianni Franchi, Ivan Donadello, Siham Tabik, David Filliat, Polícarpo Cruz, Rosana Montes, and Francisco Herrera. Explainable neural-symbolic learning (x-nesyl) methodology to fuse deep learning representations with expert knowledge graphs: the monumai cultural heritage use case. *Information Fusion*, 79:58–83, 2022.
- [22] Finale Doshi-Velez and Been Kim. Towards a rigorous science of interpretable machine learning. *ArXiv e-print*, 2017.
- [23] Alexey Dosovitskiy, Lucas Beyer, Alexander Kolesnikov, Dirk Weissenborn, Xiaohua Zhai, Thomas Unterthiner, Mostafa Dehghani, Matthias Minderer, Georg Heigold, Sylvain Gelly, et al. An image is worth 16x16 words: Transformers for image recognition at scale. *Proceedings of the International Conference on Learning Representations (ICLR)*, 2020.

[24] Michael Elad. Sparse and redundant representations: from theory to applications in signal and image processing. *Springer International Publishing*, 2010.

[25] Nelson Elhage, Tristan Hume, Catherine Olsson, Nicholas Schiefer, Tom Henighan, Shauna Kravec, Zac Hatfield-Dodds, Robert Lasenby, Dawn Drain, Carol Chen, Roger Grosse, Sam McCandlish, Jared Kaplan, Dario Amodei, Martin Wattenberg, and Christopher Olah. Toy models of superposition. *Transformer Circuits Thread*, 2022.

[26] Thomas Fel. *Sparks of explainability: recent advancements in explaining large vision models*. PhD thesis, Université de Toulouse, 2024.

[27] Thomas Fel, Remi Cadene, Mathieu Chalvidal, Matthieu Cord, David Vigouroux, and Thomas Serre. Look at the variance! efficient black-box explanations with sobol-based sensitivity analysis. *Advances in Neural Information Processing Systems (NeurIPS)*, 2021.

[28] Thomas Fel, Victor Boutin, Mazda Moayeri, Remi Cadene, Louis Bethune, Mathieu Chalvidal, and Thomas Serre. A holistic approach to unifying automatic concept extraction and concept importance estimation. *Advances in Neural Information Processing Systems (NeurIPS)*, 2023.

[29] Thomas Fel, Agustin Picard, Louis Bethune, Thibaut Boissin, David Vigouroux, Julien Colin, Rémi Cadène, and Thomas Serre. Craft: Concept recursive activation factorization for explainability. *Proceedings of the IEEE Conference on Computer Vision and Pattern Recognition (CVPR)*, 2023.

[30] Thomas Fel, Ekdeep Singh Lubana, Jacob S Prince, Matthew Kowal, Victor Boutin, Isabel Papadimitriou, Binxu Wang, Martin Wattenberg, Demba Ba, and Talia Konkle. Archetypal sae: Adaptive and stable dictionary learning for concept extraction in large vision models. *Proceedings of the International Conference on Machine Learning (ICML)*, 2025.

[31] Ruth C. Fong and Andrea Vedaldi. Interpretable explanations of black boxes by meaningful perturbation. *Proceedings of the IEEE International Conference on Computer Vision (ICCV)*, 2017.

[32] Leo Gao, Tom Dupre la Tour, Henk Tillman, Gabriel Goh, Rajan Troll, Alec Radford, Ilya Sutskever, Jan Leike, and Jeffrey Wu. Scaling and evaluating sparse autoencoders. *Proceedings of the International Conference on Learning Representations (ICLR)*, 2025.

[33] Amirata Ghorbani, Abubakar Abid, and James Zou. Interpretation of neural networks is fragile. *Proceedings of the AAAI Conference on Artificial Intelligence (AAAI)*, 2017.

[34] Amirata Ghorbani, James Wexler, James Y Zou, and Been Kim. Towards automatic concept-based explanations. *Advances in Neural Information Processing Systems (NeurIPS)*, 2019.

[35] Nicolas Gillis. *Nonnegative matrix factorization*. Springer International Publishing, 2020.

[36] Leilani H. Gilpin, David Bau, Ben Z Yuan, Ayesha Bajwa, Michael Specter, and Lalana Kagal. Explaining explanations: An overview of interpretability of machine learning. *Proceedings of the IEEE International Conference on data science and advanced analytics (DSAA)*, 2018.

[37] Liv Gorton. The missing curve detectors of inceptionv1: Applying sparse autoencoders to inceptionv1 early vision. *ArXiv e-print*, 2024.

[38] Mara Graziani, An-phi Nguyen, Laura O’Mahony, Henning Müller, and Vincent Andrearczyk. Concept discovery and dataset exploration with singular value decomposition. *Proceedings of the IEEE Conference on Computer Vision and Pattern Recognition (CVPR)*, 2023.

[39] Sorin Grigorescu, Bogdan Trasnea, Tiberiu Cocias, and Gigel Macesanu. A survey of deep learning techniques for autonomous driving. *Journal of field robotics*, 37(3): 362–386, 2020.

[40] Michael Hanna, Sandro Pezzelle, and Yonatan Belinkov. Have faith in faithfulness: Going beyond circuit overlap when finding model mechanisms. *ArXiv e-print*, 2024.

[41] Peter Hase and Mohit Bansal. Evaluating explainable ai: Which algorithmic explanations help users predict model behavior? *Proceedings of the Annual Meeting of the Association for Computational Linguistics (ACL)*, 2020.

[42] Kaiming He, Xiangyu Zhang, Shaoqing Ren, and Jian Sun. Deep residual learning for image recognition. *Proceedings of the IEEE Conference on Computer Vision and Pattern Recognition (CVPR)*, 2016.

[43] Kaiming He, Xinlei Chen, Saining Xie, Yanghao Li, Piotr Dollár, and Ross Girshick. Masked autoencoders are scalable vision learners. *Proceedings of the IEEE Conference on Computer Vision and Pattern Recognition (CVPR)*, 2022.

[44] Thomas Heap, Tim Lawson, Lucy Farnik, and Laurence Aitchison. Sparse autoencoders can interpret randomly initialized transformers. *ArXiv e-print*, 2025.

[45] Sai Sumedh R Hindupur, Ekdeep Singh Lubana, Thomas Fel, and Demba Ba. Projecting assumptions: The duality between sparse autoencoders and concept geometry. *Advances in Neural Information Processing Systems (NeurIPS)*, 2025.

[46] Cheng-Yu Hsieh, Chih-Kuan Yeh, Xuanqing Liu, Pradeep Ravikumar, Seungyeon Kim, Sanjiv Kumar, and Cho-Jui Hsieh. Evaluations and methods for explanation through robustness analysis. *Proceedings of the International Conference on Learning Representations (ICLR)*, 2021.

[47] Alon Jacovi and Yoav Goldberg. Towards faithfully interpretable nlp systems: How should we define and evaluate faithfulness? *Proceedings of the Annual Meeting of the Association for Computational Linguistics (ACL)*, 2020.

[48] Jeya Vikranth Jeyakumar, Luke Dickens, Luis Garcia, Yu-Hsi Cheng, Diego Ramirez Echavarria, Joseph Noor, Alessandra Russo, Lance Kaplan, Erik Blasch, and Mani Srivastava. Automatic concept extraction for concept bottleneck-based video classification. *ArXiv e-print*, 2022.

[49] Sonia Joseph, Praneet Suresh, Ethan Goldfarb, Lorenz Hufe, Yossi Gandalzman, Robert Graham, Danilo Bzdok, Wojciech Samek, and Blake Aaron Richards. Steering clip’s vision transformer with sparse autoencoders. *ArXiv e-print*, 2025.

[50] Sonia Joseph, Praneet Suresh, Lorenz Hufe, Edward Stevenson, Robert Graham, Yash Vadi, Danilo Bzdok, Sebastian Lapuschkin, Lee Sharkey, and Blake Aaron Richards. Prisma: An open source toolkit for mechanistic interpretability in vision and video. *ArXiv e-print*, 2025.

[51] John Jumper, Richard Evans, Alexander Pritzel, Tim Green, Michael Figurnov, Olaf Ronneberger, Kathryn Tunyasuvanakool, Russ Bates, Augustin Zidek, Anna Potapenko, et al. Highly accurate protein structure prediction with alphafold. *nature*, 596(7873):583–589, 2021.

[52] Rémi Kazmierczak, Eloïse Berthier, Goran Frehse, and Gianni Franchi. Clip-qda: An explainable concept bottleneck model. *The Journal of Transactions on Machine Learning Research (TMLR)*, 2023.

[53] Been Kim, Martin Wattenberg, Justin Gilmer, Carrie Cai, James Wexler, Fernanda Viegas, et al. Interpretability beyond feature attribution: Quantitative testing with concept activation vectors (tcav). *Proceedings of the International Conference on Machine Learning (ICML)*, 2018.

[54] Eunji Kim, Dahuin Jung, Sangha Park, Siwon Kim, and Sungroh Yoon. Probabilistic concept bottleneck models. *Proceedings of the International Conference on Machine Learning (ICML)*, 2023.

[55] Sunnie S. Y. Kim, Nicole Meister, Vikram V. Ramaswamy, Ruth Fong, and Olga Russakovsky. HIVE: Evaluating the human interpretability of visual explanations. *Proceedings of the IEEE European Conference on Computer Vision (ECCV)*, 2022.

[56] David Klindt, Lukas Schott, Yash Sharma, Ivan Ustyuzhaninov, Wieland Brendel, Matthias Bethge, and Dylan Paiton. Towards nonlinear disentanglement in natural data with temporal sparse coding. *ArXiv e-print*, 2020.

[57] David Klindt, Sophia Sanborn, Francisco Acosta, Frederic Poitevin, and Nina Miolane. Identifying interpretable visual features in artificial and biological neural systems. *ArXiv e-print*, 2023.

[58] David Klindt, Charles O’Neill, Patrik Reizinger, Harald Maurer, and Nina Miolane. From superposition to sparse codes: interpretable representations in neural networks. *ArXiv e-print*, 2025.

[59] Pang Wei Koh, Thao Nguyen, Yew Siang Tang, Stephen Mussmann, Emma Pierson, Been Kim, and Percy Liang. Concept bottleneck models. *Proceedings of the International Conference on Machine Learning (ICML)*, 2020.

[60] Matthew Kowal, Achal Dave, Rares Ambrus, Adrien Gaidon, Konstantinos G Derpanis, and Pavel Tokmakov. Understanding video transformers via universal concept discovery. *Proceedings of the IEEE Conference on Computer Vision and Pattern Recognition (CVPR)*, 2024.

[61] Matthew Kowal, Richard P Wildes, and Konstantinos G Derpanis. Visual concept connectome (vcc): Open world concept discovery and their interlayer connections in deep models. *Proceedings of the IEEE Conference on Computer Vision and Pattern Recognition (CVPR)*, 2024.

[62] Yann LeCun, Yoshua Bengio, and Geoffrey Hinton. Deep learning. *Nature*, 2015.

[63] Francesco Locatello, Stefan Bauer, Mario Lucic, Gunnar Raetsch, Sylvain Gelly, Bernhard Scholkopf, and Olivier Bachem. Challenging common assumptions in the unsupervised learning of disentangled representations. *Proceedings of the International Conference on Machine Learning (ICML)*, 2019.

[64] Alireza Makhzani and Brendan Frey. K-sparse autoencoders. *Proceedings of the International Conference on Learning Representations (ICLR)*, 2014.

[65] Andrei Margelioiu, Matthew Ashman, Umang Bhatt, Yanzhi Chen, Mateja Jamnik, and Adrian Weller. Do concept bottleneck models learn as intended? *arXiv preprint arXiv:2105.04289*, 2021.

[66] Mazda Moayeri, Keivan Rezaei, Maziar Sanjabi, and Soheil Feizi. Text-to-concept (and back) via cross-model alignment. *Proceedings of the International Conference on Machine Learning (ICML)*, 2023.

[67] Sabine Muzellec, Leo Andeol, Thomas Fel, Rufin Van-Rullen, and Thomas Serre. Gradient strikes back: How filtering out high frequencies improves explanations. *Proceedings of the International Conference on Learning Representations (ICLR)*, 2024.

[68] Giang Nguyen, Daeyoung Kim, and Anh Nguyen. The effectiveness of feature attribution methods and its correlation with automatic evaluation scores. *Advances in Neural Information Processing Systems (NeurIPS)*, 2021.

[69] Paul Novello, Thomas Fel, and David Vigouroux. Making sense of dependence: Efficient black-box explanations using dependence measure. *Advances in Neural Information Processing Systems (NeurIPS)*, 2022.

[70] Tuomas Oikarinen and Tsui-Wei Weng. Clip-dissect: Automatic description of neuron representations in deep vision networks. *Proceedings of the International Conference on Learning Representations (ICLR)*, 2023.

[71] Tuomas Oikarinen, Subhro Das, Lam M Nguyen, and Tsui-Wei Weng. Label-free concept bottleneck models. *Proceedings of the International Conference on Learning Representations (ICLR)*, 2023.

[72] Maxime Oquab, Timothée Darcet, Théo Moutakanni, Huy Vo, Marc Szafraniec, Vasil Khalidov, Pierre Fernandez, Daniel Haziza, Francisco Massa, Alaaddin El-Nouby, et al. Dinov2: Learning robust visual features without supervision. *ArXiv e-print*, 2023.

[73] Konstantinos Panousis and Sotirios Chatzis. Discover: making vision networks interpretable via competition and dissection. *Advances in Neural Information Processing Systems (NeurIPS)*, 2023.

[74] Isabel Papadimitriou, Huangyuan Su, Thomas Fel, Sham Kakade, and Stephanie Gil. Interpreting the linear structure of vision-language model embedding spaces. *Proceedings of the Conference on Language Modeling (COLM)*, 2025.

[75] Jayneel Parekh, Pegah Khayatan, Mustafa Shukor, Alasdair Newson, and Matthieu Cord. A concept-based explainability framework for large multimodal models. *ArXiv e-print*, 2024.

[76] Kiho Park, Yo Joong Choe, and Victor Veitch. The linear representation hypothesis and the geometry of large language models. *Proceedings of the International Conference on Machine Learning (ICML)*, 2024.

[77] Adam Paszke, Sam Gross, Francisco Massa, Adam Lerer, James Bradbury, Gregory Chanan, Trevor Killeen, Zeming Lin, Natalia Gimelshein, Luca Antiga, et al. Pytorch: An imperative style, high-performance deep learning library. *Ad-*

vances in Neural Information Processing Systems (NeurIPS), 2019.

[78] Goncalo Paulo and Nora Belrose. Sparse autoencoders trained on the same data learn different features. *ArXiv e-print*, 2025.

[79] Eleonora Poeta, Gabriele Ciravegna, Eliana Pastor, Tania Cerquitelli, and Elena Baralis. Concept-based explainable artificial intelligence: A survey. *ArXiv e-print*, 2023.

[80] Senthooran Rajamanoharan, Tom Lieberum, Nicolas Sonnerat, Arthur Conmy, Vikrant Varma, Janos Kramar, and Neel Nanda. Jumping ahead: Improving reconstruction fidelity with jumprelu sparse autoencoders. *ArXiv e-print*, 2024.

[81] Sukrut Rao, Sweta Mahajan, Moritz Böhle, and Bernt Schiele. Discover-then-name: Task-agnostic concept bottlenecks via automated concept discovery. *Proceedings of the IEEE European Conference on Computer Vision (ECCV)*, 2024.

[82] Karsten Roth, Jae Myung Kim, Andrew Koepke, Oriol Vinyals, Cordelia Schmid, and Zeynep Akata. Waffling around for performance: Visual classification with random words and broad concepts. *Proceedings of the IEEE Conference on Computer Vision and Pattern Recognition (CVPR)*, 2023.

[83] Olga Russakovsky, Jia Deng, Hao Su, Jonathan Krause, Sanjeev Satheesh, Sean Ma, Zhiheng Huang, Andrej Karpathy, Aditya Khosla, Michael Bernstein, et al. Imagenet large scale visual recognition challenge. *International journal of computer vision*, 115(3):211–252, 2015.

[84] Waddah Saeed and Christian Omlin. Explainable ai (xai): A systematic meta-survey of current challenges and future opportunities. *Knowledge-Based Systems*, 2023.

[85] Ramprasaath R. Selvaraju, Michael Cogswell, Abhishek Das, Ramakrishna Vedantam, Devi Parikh, and Dhruv Batra. Grad-cam: Visual explanations from deep networks via gradient-based localization. *Proceedings of the IEEE International Conference on Computer Vision (ICCV)*, 2017.

[86] Thomas Serre. Deep learning: The good, the bad, and the ugly. *Annual review of vision science*, 2019.

[87] Mustafa Shukor and Matthieu Cord. Implicit multimodal alignment: On the generalization of frozen llms to multimodal inputs. *ArXiv e-print*, 2024.

[88] Karen Simonyan, Andrea Vedaldi, and Andrew Zisserman. Deep inside convolutional networks: Visualising image classification models and saliency maps. *Proceedings of the International Conference on Learning Representations (ICLR)*, 2013.

[89] Leon Sixt, Maximilian Granz, and Tim Landgraf. When explanations lie: Why many modified bp attributions fail. *Proceedings of the International Conference on Machine Learning (ICML)*, 2020.

[90] Daniel Smilkov, Nikhil Thorat, Been Kim, Fernanda Viégas, and Martin Wattenberg. Smoothgrad: removing noise by adding noise. *Proceedings of the International Conference on Machine Learning (ICML)*, 2017.

[91] Jost Tobias Springenberg, Alexey Dosovitskiy, Thomas Brox, and Martin Riedmiller. Striving for simplicity: The all convolutional net. *Workshop Proceedings of the International Conference on Learning Representations (ICLR)*, 2014.

[92] Divyansh Srivastava, Ge Yan, and Lily Weng. Vlg-cbm: Training concept bottleneck models with vision-language guidance. *Advances in Neural Information Processing Systems*, 37:79057–79094, 2024.

[93] Mukund Sundararajan, Ankur Taly, and Qiqi Yan. Axiomatic attribution for deep networks. *Proceedings of the International Conference on Machine Learning (ICML)*, 2017.

[94] Andong Tan, Fengtao Zhou, and Hao Chen. Explain via any concept: Concept bottleneck model with open vocabulary concepts. *Proceedings of the IEEE European Conference on Computer Vision (ECCV)*, 2024.

[95] Adly Templeton, Tom Conerly, Jonathan Marcus, Jack Lindsey, Trenton Bricken, Brian Chen, Adam Pearce, Craig Citro, Emmanuel Ameisen, Andy Jones, Hoagy Cunningham, Nicholas L Turner, Callum McDougall, Monte MacDiarmid, C. Daniel Freeman, Theodore R. Sumers, Edward Rees, Joshua Batson, Adam Jermyn, Shan Carter, Chris Olah, and Tom Henighan. Scaling monosemanticity: Extracting interpretable features from claude 3 sonnet. *Transformer Circuits Thread*, 2024.

[96] Robert Tibshirani. Regression shrinkage and selection via the lasso. *Journal of the Royal Statistical Society Series B: Statistical Methodology*, 1996.

[97] Jessica Vamathevan, Dominic Clark, Paul Czodrowski, Ian Dunham, Edgardo Ferran, George Lee, Bin Li, Anant Madabhushi, Parantu Shah, Michaela Spitzer, et al. Applications of machine learning in drug discovery and development. *Nature reviews Drug discovery*, 18(6):463–477, 2019.

[98] Moritz Vandenhirtz, Sonia Laguna, Ricards Marcinkevics, and Julia Vogt. Stochastic concept bottleneck models. *Advances in Neural Information Processing Systems (NeurIPS)*, 2024.

[99] Johanna Vielhaben, Stefan Blücher, and Nils Strothoff. Multi-dimensional concept discovery (mcd): A unifying framework with completeness guarantees. *The Journal of Transactions on Machine Learning Research (TMLR)*, 2023.

[100] Catherine Wah, Steve Branson, Peter Welinder, Pietro Perona, and Serge Belongie. The caltech-ucsd birds-200-2011 dataset. 2011.

[101] Daan Wynen, Cordelia Schmid, and Julien Mairal. Unsupervised learning of artistic styles with archetypal style analysis. *Advances in Neural Information Processing Systems (NeurIPS)*, 2018.

[102] Mert Yuksekogul, Maggie Wang, and James Zou. Post-hoc concept bottleneck models. *Proceedings of the International Conference on Learning Representations (ICLR)*, 2023.

[103] Matthew D Zeiler and Rob Fergus. Visualizing and understanding convolutional networks. *Proceedings of the IEEE European Conference on Computer Vision (ECCV)*, 2014.

[104] Xiaohua Zhai, Alexander Kolesnikov, Neil Houlsby, and Lucas Beyer. Scaling vision transformers. *Proceedings of the IEEE Conference on Computer Vision and Pattern Recognition (CVPR)*, 2022.

[105] Xiaohua Zhai, Basil Mustafa, Alexander Kolesnikov, and Lucas Beyer. Sigmoid loss for language image pre-training.

Proceedings of the IEEE International Conference on Computer Vision (ICCV), 2023.

[106] Ruihan Zhang, Prashan Madumal, Tim Miller, Krista A Ehinger, and Benjamin IP Rubinstein. Invertible concept-based explanations for cnn models with non-negative concept activation vectors. *Proceedings of the AAAI Conference on Artificial Intelligence (AAAI)*, 2021.

A Geometric Unification of Concept Learning with Concept Cones

Supplementary Material

A. Detailed CBM Variant Descriptions

In this section, we provide comprehensive descriptions of each CBM variant presented in Equation 3, clarifying their specific architectures, training procedures, and key distinctions.

A.1. Joint and Sequential CBM

Joint CBM [59]. The original CBM formulation where both the concept prediction layer \mathbf{W}_c and the task prediction layer \mathbf{W}_y are trained simultaneously with $\lambda > 0$. The model minimizes both concept prediction loss (via binary cross-entropy on labeled concepts c_i) and task prediction loss (via cross-entropy on labels y_i) jointly. This requires a dataset with both concept annotations and task labels. The joint training allows the model to learn concepts that are both semantically meaningful and maximally useful for the downstream task, but may lead to concepts that are less faithful to their intended human interpretation.

Sequential CBM [59]. A two-stage training procedure where the concept layer \mathbf{W}_c is first trained to predict concept labels (stage 1), then frozen, and the task prediction layer \mathbf{W}_y is trained on top of the predicted concepts (stage 2). This approach enforces a stricter bottleneck since the task predictor can only access information through the learned concepts, potentially improving interpretability at the cost of some task performance. Sequential training ensures concepts remain faithful to their annotations, as they are optimized solely for concept prediction in the first stage.

Independent CBM [59]. Concept and task predictors are trained completely independently: \mathbf{W}_c is trained to predict concepts, and \mathbf{W}_y is trained directly on the original features \mathbf{a}_i to predict tasks. At inference time, the independently trained components are composed: predictions flow through \mathbf{W}_c to produce concepts, which are then fed to \mathbf{W}_y . This variant is primarily used for analysis and comparison rather than practical deployment.

A.2. Label-Free CBM (LF-CBM)

Method [71]. Label-Free CBM eliminates the need for concept annotations ($\lambda = 0$) by leveraging large language models (LLMs) to generate task-relevant concepts. Given class names, GPT-3 is prompted to generate a set of discriminative concepts for each class (e.g., "red feathers," "curved beak" for bird species). These textual concepts are embedded using CLIP's text encoder to obtain $\mathbf{D}_{\text{LLM}} \in \mathbb{R}^{c \times d}$. The concept prediction layer is then defined as $\mathbf{W}_c = \mathbf{D}_{\text{LLM}}$, and

the model learns to align image features to these text-derived concept directions.

Architecture Details. For an input image x_i , the model computes:

$$\mathbf{a}_i = \mathbf{f}(x_i) \quad (\text{CLIP image features}) \quad (13)$$

$$\hat{\mathbf{c}}_i = \sigma(\mathbf{a}_i \mathbf{D}_{\text{LLM}}^\top + \mathbf{b}_c) \quad (\text{concept predictions}) \quad (14)$$

$$\hat{\mathbf{y}}_i = \text{softmax}(\hat{\mathbf{c}}_i \mathbf{W}_y^\top + \mathbf{b}_y) \quad (\text{class predictions}) \quad (15)$$

The model is trained end-to-end with only task labels, learning to activate the "correct" LLM-generated concepts for classification.

Limitations. There is no guarantee that LLM-generated concepts are actually detectable in the learned features \mathbf{f} , potentially leading to unfaithful explanations where concept activations do not correspond to their semantic meaning [65, 82].

A.3. Post-hoc CBM

Method [102]. Post-hoc CBM constructs concept bottlenecks from already-trained neural networks without retraining. Given a trained feature extractor \mathbf{f} and a set of labeled concept examples, the method learns a linear concept bank \mathbf{D}_{Bank} that decomposes feature activations into interpretable directions.

Concept Bank Construction. Several approaches can be used:

- **Supervised projection:** For each concept, collect positive and negative examples, compute their mean features, and define the concept direction as the normalized difference.
- **Matrix factorization:** Apply PCA, NMF, or ICA to activation matrices to discover latent directions, then label them post-hoc.
- **Probe training:** Train linear probes on features to predict binary concept labels, using probe weights as concept directions.

Architecture with Residual. A key variant of Post-hoc CBM includes a residual connection to preserve information:

$$\hat{\mathbf{c}}_i = \sigma(\mathbf{a}_i \mathbf{D}_{\text{Bank}}^\top + \mathbf{b}_c) \quad (16)$$

$$\hat{\mathbf{y}}_i = \text{softmax}([\hat{\mathbf{c}}_i \mid \mathbf{a}_i] \mathbf{W}_y^\top + \mathbf{b}_y) \quad (17)$$

where $[\hat{\mathbf{c}}_i \mid \mathbf{a}_i]$ denotes concatenation. The residual connection allows the model to maintain original task performance

while providing concept-based explanations, at the cost of reduced faithfulness to the bottleneck constraint.

A.4. DN-CBM (Discover-then-Name CBM)

Method [81]. DN-CBM inverts the traditional CBM paradigm by first discovering concepts the model has learned, then naming them, and finally using them for classification. The method uses Sparse Autoencoders (SAEs) to decompose CLIP features into interpretable concept directions in an unsupervised, task-agnostic manner.

Concept Discovery via SAE. An SAE is trained to reconstruct CLIP features with sparsity constraints:

$$\mathcal{L}_{\text{SAE}}(\mathbf{a}) = \|\text{SAE}(\mathbf{a}) - \mathbf{a}\|_2^2 + \lambda_1 \|\phi(f(\mathbf{a}))\|_1 \quad (18)$$

where $f(\mathbf{a}) = \mathbf{W}_E^\top \mathbf{a}$ is the encoder, ϕ is ReLU, and $g(\cdot) = \mathbf{W}_D^\top \phi(f(\mathbf{a}))$ is the decoder. The dictionary $\mathbf{D}_{\text{SAE}} = \mathbf{W}_D \in \mathbb{R}^{c \times d}$ contains learned concept directions as rows.

Automated Concept Naming. Each SAE neuron (dictionary atom) is assigned a name by finding the closest text embedding in CLIP space:

$$s_c = \arg \min_{v \in \mathcal{V}} \cos(\mathbf{p}_c, \text{CLIP}_{\text{text}}(v)) \quad (19)$$

where $\mathbf{p}_c = [\mathbf{W}_D]_c$ is the dictionary vector and \mathcal{V} is a vocabulary (e.g., 20k common English words).

Task-Agnostic Bottleneck. The SAE is trained once on a large unlabeled dataset (e.g., CC3M), then frozen and used as a concept bottleneck for multiple downstream tasks:

$$\hat{\mathbf{c}}_i = \phi(\mathbf{a}_i \mathbf{D}_{\text{SAE}}^\top) \quad (\text{sparse concept activations}) \quad (20)$$

$$\hat{y}_i = \text{softmax}(\hat{\mathbf{c}}_i \mathbf{W}_y^\top + \mathbf{b}_y) \quad (\text{task-specific linear classifier}) \quad (21)$$

Only the linear classifier \mathbf{W}_y is trained per task, making DN-CBM highly efficient and scalable.

A.5. SpLiCE (Sparse Linear Concept Embeddings)

Method [8]. SpLiCE interprets CLIP models by decomposing image features into sparse linear combinations of pre-defined text concept embeddings. Unlike DN-CBM which learns the dictionary, SpLiCE uses a fixed dictionary $\mathbf{D}_{\text{CLIP}}^\top$ consisting of CLIP text embeddings of a concept vocabulary.

Architecture. For each image, SpLiCE solves an optimization problem to find sparse concept coefficients:

$$\hat{\mathbf{c}}_i = \arg \min_c \|\mathbf{a}_i - \mathbf{D}_{\text{CLIP}}^\top \mathbf{c}\|_2^2 + \lambda \|\mathbf{c}\|_1 \quad (22)$$

where $\mathbf{a}_i = \text{CLIP}_{\text{image}}(\mathbf{x}_i)$ and $\mathbf{D}_{\text{CLIP}}^\top \in \mathbb{R}^{d \times c}$ contains CLIP text embeddings as columns.

Key Distinction. SpLiCE is primarily an *interpretation* method rather than a classification model. The sparse codes $\hat{\mathbf{c}}_i$ explain what concepts CLIP "sees" in an image, but are not used to train a downstream classifier. The method is post-hoc and does not require retraining the feature extractor.

A.6. Stochastic CBM

Method [98]. Stochastic CBM (also called Probabilistic CBM [54]) replaces deterministic concept predictions with distributions to capture uncertainty.

Architecture. Instead of directly predicting concept activations, the model learns parameters of a Gaussian distribution:

$$\boldsymbol{\mu}(\mathbf{a}_i) = \mathbf{W}_\mu^\top \mathbf{a}_i + \mathbf{b}_\mu \quad (23)$$

$$\boldsymbol{\Sigma}(\mathbf{a}_i) = \text{softplus}(\mathbf{W}_\Sigma^\top \mathbf{a}_i + \mathbf{b}_\Sigma) \quad (24)$$

$$\boldsymbol{\eta}_i \sim \mathcal{N}(\boldsymbol{\mu}(\mathbf{a}_i), \text{diag}(\boldsymbol{\Sigma}(\mathbf{a}_i))) \quad (25)$$

$$\hat{\mathbf{c}}_i = \sigma(\boldsymbol{\eta}_i) \quad (26)$$

During training, samples are drawn from $\mathcal{N}(\boldsymbol{\mu}, \boldsymbol{\Sigma})$ and passed through the sigmoid to produce concept probabilities. At inference, the mean $\boldsymbol{\mu}(\mathbf{a}_i)$ can be used, or multiple samples can be drawn to quantify prediction uncertainty.

Concept Directions. The concept directions are encoded in \mathbf{W}_μ , which can be viewed as \mathbf{W}_c in the deterministic case. The stochasticity allows the model to express when it is uncertain about a concept's presence, improving calibration and intervention efficacy.

A.7. CLIP-QDA

Method [52]. CLIP-QDA constructs an interpretable concept bottleneck using Quadratic Discriminant Analysis (QDA) in a concept space derived from CLIP text embeddings.

Concept Space Construction.

1. Start with a vocabulary \mathcal{V} of concept words (e.g., 20k common English words)
2. Embed each word using CLIP text encoder: $t_i = \text{CLIP}_{\text{text}}(v_i)$
3. Apply PCA to reduce dimensionality: $\mathbf{D}_{\text{CLIP}} = \text{PCA}(\{t_1, \dots, t_{|\mathcal{V}|}\}) \in \mathbb{R}^{c \times d}$
4. For an image, compute concept representation: $\hat{\mathbf{c}}_i = \mathbf{a}_i^\top \mathbf{D}_{\text{CLIP}}^\top$

Quadratic Discriminant Analysis. Instead of learning a linear classifier \mathbf{W}_y , CLIP-QDA learns class-specific Gaussian distributions:

$$p(\hat{\mathbf{c}} | y) = \mathcal{N}(\boldsymbol{\mu}_y, \boldsymbol{\Sigma}_y) \quad (27)$$

$$\hat{y}_i = \arg \max_y [\log p(\hat{\mathbf{c}}_i | y) + \log p(y)] \quad (28)$$

This results in quadratic decision boundaries in concept space, which can model more complex class distributions than linear CBMs.

B. Concept Cones: A Unifying Geometric Framework.

We provide a detailed proof of Proposition 1, which establishes that concept cones provide a unifying geometric framework for both supervised (CBM) and unsupervised (SAE, CRAFT, etc.) concept extraction methods.

We recall our setup with our activation space: $\mathcal{A} \subset \mathbb{R}^d$, with activations $\mathbf{a}_i = \mathbf{f}(\mathbf{x}_i)$, the concept dictionary: $\mathbf{D} \in \mathbb{R}^{c \times d}$ (rows are concept directions) and the associated concept codes: $\mathbf{z}_i \in \mathbb{R}^c$ (unsupervised) or $\hat{\mathbf{c}}_i \in [0, 1]^c$ (supervised). We denote the concept cone: $\mathcal{C}_{\mathbf{D}} = \{\mathbf{v} \in \mathbb{R}^d : \mathbf{v} = \boldsymbol{\alpha}^\top \mathbf{D}, \boldsymbol{\alpha} \in \mathbb{R}_+^c\}$. For unsupervised methods (Equation 2), the objective is:

$$\min_{\mathbf{Z}, \mathbf{D}} \|\mathbf{A} - \mathbf{ZD}\|_F^2 + \Omega(\mathbf{Z}, \mathbf{D}) \quad (29)$$

where $\Omega(\cdot)$ encodes constraints (sparsity, nonnegativity, or orthogonality, etc.), see Equation (2) or details.

For supervised methods (Equation (3)), the objective is:

$$\min_{\mathbf{W}_c, \mathbf{W}_y} \frac{1}{n} \sum_{i=1}^n \mathcal{L}_{\text{CE}}(\hat{\mathbf{y}}_i, \mathbf{y}_i) + \lambda \mathcal{L}_{\text{BCE}}(\hat{\mathbf{c}}_i, \mathbf{c}_i) \quad (30)$$

where $\hat{\mathbf{c}}_i = \sigma(\mathbf{a}_i \mathbf{W}_c^\top + \mathbf{b}_c)$ and $\hat{\mathbf{y}}_i = \text{softmax}(\hat{\mathbf{c}}_i \mathbf{W}_y^\top + \mathbf{b}_y)$. See Equation (3) and Sec. A for details. We recall our claim:

Observation 2 (Concept Cones Unify Extraction Methods). *Let $\mathbf{D} \in \mathbb{R}^{c \times d}$ be a concept dictionary learned by any method in Equation (2) or Equation (3). Then:*

- (i) **Projection operator:** Both supervised and unsupervised methods implicitly learn a projection operator $\Pi_{\mathcal{C}_{\mathbf{D}}} : \mathbb{R}^d \rightarrow \mathcal{C}_{\mathbf{D}}$ that maps activations onto the concept cone via $\Pi_{\mathcal{C}_{\mathbf{D}}}(\mathbf{a}) = \hat{\mathbf{c}}^\top \mathbf{D}$ where $\hat{\mathbf{c}} \geq 0$.
- (ii) **Shared geometric structure:** Supervised methods (CBMs) and unsupervised methods optimize for different objectives—task performance vs. reconstruction—but both search for a convex cone $\mathcal{C}_{\mathbf{D}}$ in activation space that captures the relevant subspace of \mathcal{A} .
- (iii) **Concept recoverability:** A concept direction $\mathbf{v} \in \mathbb{R}^d$ learned by one method is recoverable from dictionary \mathbf{D} learned by another if and only if $\mathbf{v} \in \mathcal{C}_{\mathbf{D}}$, i.e., there exists $\boldsymbol{\alpha} \in \mathbb{R}_+^c$ such that $\mathbf{v} = \boldsymbol{\alpha}^\top \mathbf{D}$. Agreement between methods is thus quantified by their cone overlap.

Proof. (i): Projection Operators

We first show that, for any unsupervised method in Equation 2 that enforces $\mathbf{Z} \geq 0$ (e.g., SAE with ReLU, CRAFT

with nonnegativity, NMF), the reconstruction $\hat{\mathbf{a}}_i = \mathbf{z}_i^\top \mathbf{D}$ lies in the concept cone $\mathcal{C}_{\mathbf{D}}$.

By definition, $\hat{\mathbf{a}}_i = \mathbf{z}_i^\top \mathbf{D} = \sum_{j=1}^c z_{ij} \mathbf{D}_j$ where \mathbf{D}_j is the j -th row of \mathbf{D} . Since the constraint ensures $\mathbf{z}_i \geq 0$ (either explicitly via $\mathbf{Z} \geq 0$ in CRAFT/NMF, or implicitly via $\phi(\cdot) = \text{ReLU}(\cdot)$ in SAEs), we have $z_{ij} \geq 0$ for all j . Therefore, $\hat{\mathbf{a}}_i$ is a nonnegative linear combination of the rows of \mathbf{D} , which by definition means $\hat{\mathbf{a}}_i \in \mathcal{C}_{\mathbf{D}}$. Thus, the mapping $\mathbf{a}_i \mapsto \hat{\mathbf{a}}_i$ defines a (possibly approximate) projection $\Pi_{\mathcal{C}_{\mathbf{D}}} : \mathbb{R}^d \rightarrow \mathcal{C}_{\mathbf{D}}$.

Similarly, we now show that for CBMs (Equation 3), the bottleneck representation $\hat{\mathbf{a}}_i = \hat{\mathbf{c}}_i^\top \mathbf{W}_c$ lies in the concept cone $\mathcal{C}_{\mathbf{W}_c}$. Since in a CBM, concept predictions are $\hat{\mathbf{c}}_i = \sigma(\mathbf{a}_i \mathbf{W}_c^\top + \mathbf{b}_c)$ where σ is the sigmoid (or other activation ensuring $[0, 1]$ output). By definition of sigmoid, $\hat{c}_{ij} \in [0, 1] \subset \mathbb{R}_+$ for all j . The bottleneck representation that is fed to the classifier is:

$$\hat{\mathbf{a}}_i = \hat{\mathbf{c}}_i^\top \mathbf{W}_c = \sum_{j=1}^c \hat{c}_{ij} (\mathbf{W}_c)_j \quad (31)$$

where $(\mathbf{W}_c)_j$ is the j -th row of \mathbf{W}_c . Since $\hat{c}_{ij} \geq 0$, this is a nonnegative linear combination of concept directions, hence $\hat{\mathbf{a}}_i \in \mathcal{C}_{\mathbf{W}_c}$. The mapping $\mathbf{a}_i \mapsto \hat{\mathbf{a}}_i$ defines a projection (in the sense of dimension reduction through the bottleneck) onto the concept cone.

Both paradigms produce representations that lie in concept cones, defining implicit projection operators $\Pi_{\mathcal{C}_{\mathbf{D}}}$.

(ii): Shared Geometric Structure

We start with unsupervised method and show that they select a cone $\mathcal{C}_{\mathbf{D}}$ to minimize reconstruction error: $\min_{\mathbf{D}} \mathbb{E}_{\mathbf{a} \sim P_A} [\|\mathbf{a} - \Pi_{\mathcal{C}_{\mathbf{D}}}(\mathbf{a})\|^2]$ subject to sparsity/structure constraints on codes. The objective in Equation 29 can be written per-sample as:

$$\mathcal{L}_{\text{unsup}}(\mathbf{a}_i) = \min_{\mathbf{z}_i \geq 0} \|\mathbf{a}_i - \mathbf{z}_i^\top \mathbf{D}\|^2 + \Omega(\mathbf{z}_i) \quad (32)$$

The optimal code \mathbf{z}_i^* produces the reconstruction $\hat{\mathbf{a}}_i = \mathbf{z}_i^{*\top} \mathbf{D} \in \mathcal{C}_{\mathbf{D}}$. Since $\mathbf{z}_i^* = \arg \min_{\mathbf{z} \geq 0} \|\mathbf{a}_i - \mathbf{z}^\top \mathbf{D}\|^2 + \Omega(\mathbf{z})$, the reconstruction $\hat{\mathbf{a}}_i$ is the best approximation of \mathbf{a}_i within the cone $\mathcal{C}_{\mathbf{D}}$ under the given regularization. Optimizing over \mathbf{D} thus amounts to selecting the cone that minimizes expected reconstruction error over the data distribution.

We now turn to unsupervised methods and show that CBMs select a cone $\mathcal{C}_{\mathbf{W}_c}$ to maximize task performance: $\min_{\mathbf{W}_c} \mathbb{E}_{(\mathbf{a}, y) \sim P} [\mathcal{L}_{\text{CE}}(h(\Pi_{\mathcal{C}_{\mathbf{W}_c}}(\mathbf{a})), y)]$ where h is the task classifier. We note that the CBM objective in Equation 30 can be decomposed as:

$$\mathcal{L}_{\text{CBM}} = \mathbb{E}_{(\mathbf{a}, y)} [\mathcal{L}_{\text{CE}}(\text{softmax}(\hat{\mathbf{c}}^\top \mathbf{W}_y), y)] + \lambda \mathbb{E}_{(\mathbf{a}, \mathbf{c})} [\mathcal{L}_{\text{BCE}}(\hat{\mathbf{c}}, \mathbf{c})] \quad (33)$$

$$= \mathbb{E}_{(\mathbf{a}, y)} [\mathcal{L}_{\text{CE}}(h(\hat{\mathbf{c}}^\top \mathbf{W}_c), y)] + \lambda \mathbb{E} [\mathcal{L}_{\text{BCE}}(\hat{\mathbf{c}}, \mathbf{c})] \quad (34)$$

where $\hat{\mathbf{c}}^\top \mathbf{W}_c \in \mathcal{C}_{\mathbf{W}_c}$ is the bottleneck representation. The first term optimizes the cone $\mathcal{C}_{\mathbf{W}_c}$ such that projections onto it preserve task-relevant information. The second term (when $\lambda > 0$) biases the cone toward human-interpretable concept directions, but the primary driver is task loss. Thus, supervised methods select the cone that best supports downstream classification, as opposed to reconstruction.

Thus, both paradigms optimize for a convex cone \mathcal{C}_D in activation space, but under different criteria: unsupervised methods prioritize reconstruction fidelity, while supervised methods prioritize task discrimination. The geometric structure—a cone generated by nonnegative combinations of concept directions—is identical, only the selection criterion differs.

(iii): Concept Recoverability We now show that a concept direction $\mathbf{w} \in \mathbb{R}^d$ is recoverable from dictionary \mathbf{D} if and only if $\mathbf{w} \in \mathcal{C}_D$. If \mathbf{w} is recoverable, then $\mathbf{w} \in \mathcal{C}_D$: Suppose \mathbf{w} is recoverable from \mathbf{D} , meaning there exists a code $\alpha \geq 0$ such that $\mathbf{w} = \alpha^\top \mathbf{D}$. By definition of the concept cone (Equation 4), this implies $\mathbf{w} \in \mathcal{C}_D$. Similarly, if $\mathbf{w} \in \mathcal{C}_D$, then \mathbf{w} is recoverable. We note the contrapositive: if $\mathbf{w} \notin \mathcal{C}_D$, then no nonnegative combination of \mathbf{D} 's rows can produce \mathbf{w} , hence \mathbf{w} is not recoverable from \mathbf{D} . \square

This geometric view makes precise the intuition that both supervised and unsupervised methods "carve out" a subspace of activation space, constrained to be a convex cone due to nonnegativity, and differing only in *which* cone they select based on their optimization objective.

C. Experimental Settings

C.1. Concept Bottleneck Model architecture

The CBM branch is constructed in parallel to the SAE branch and operates on the same frozen backbone layer. Each CBM consists of two components. First, a feature-to-concept predictor W_c maps backbone activations to M concept logits, which are converted into probabilities through a sigmoid. Second, a bias-free linear classifier W_y maps the predicted concept vector to class logits. We evaluate three backbones: (i) **ResNet-50**, where the CBM/SAE is applied after global average pooling for a given layer; (ii) **ViT-B/16**; and (iii) **DINO-v2 ViT-B/14**, where both CBM and SAE operate on the class token.

CUB. For CUB, we use the human-annotated bird attributes. Uncertain image-level annotations are removed and the remaining labels are aggregated into class-level binary concepts via majority vote. Following prior work [59], we retain only attributes that appear in a sufficient number of classes. Out of 312 attributes, 168 pass this filtering. We jointly train W_c and W_y using a binary cross-entropy loss

on the concepts and a cross-entropy loss on the class logits. We trained each backbone under its own optimized schedule: ResNet-50 was trained for 75 epochs with a learning rate of 0.01, ViT was trained for 50 epochs with a learning rate of 0.01, and DINO was loaded from **DINO-v2 ViT-B/14** and frozen, then a linear probing layer was trained for 50 epochs with a learning rate of 0.01. However, we plug the SAE on the CLS-token.

ImageNet. For ImageNet, we rely on the VLG-CBM concepts introduced in [92]. These concepts are obtained via a VLLM annotation pipeline that also provides an uncertainty score for each concept. After thresholding by confidence and aggregating image-level labels into class-level concepts via majority vote, we retain 3545 concepts out of the original 5305 using the same strategy as that of CUB. Training again optimizes both concept prediction and class classification via the combined loss (similar to what we on for CUB's dataset).

For each backbone, we loaded weights. For ResNet50, we use "*IMAGENET1K_V2*" weights. For ViT-B/16, we use "*IMAGENET1K_V1*" weights from Pytorch [77]. We load **DINO-v2 ViT-B/14** for the DINO backbone.

Concept Selection and Performance. The curated concept sets for both datasets allow the CBM to achieve strong predictive accuracy across backbones. Table A.3 compares our results to two baselines: P-CBM [102] and Label-Free CBM [71]. Our CBM consistently outperforms prior approaches, and the improvements hold across all architectures.

On **CUB**, our DINO-v2 CBM reaches **84.39%**, outperforming the Label-Free CBM (74.31%) by over ten points and substantially surpassing the P-CBM baseline (59.60%). ResNet-50 and ViT-B/16 also achieve solid performance (72.79% and 69.70%, respectively), confirming that our concept selection and training pipeline generalizes across architectures.

On **ImageNet**, our CBM achieves **77-80%** accuracy across backbones. DINO-v2 again yields the strongest result with **80.30%**, clearly improving over the Label-Free CBM baseline (71.95%). These high scores indicate that the learned concepts provide meaningful supervision even on a large and diverse dataset.

Overall, the table confirms that our CBM implementation is competitive with and often superior to previous CBM frameworks. Combined with the SAE results, this supports the conclusion that our CBMs form a reliable reference geometry for evaluating the alignment between supervised concepts and unsupervised sparse representations.

Table A.3. Comparison of CBM across datasets.

Model	Dataset	
	CUB200	ImageNet
P-CBM	59.60%	N/A
Label-free CBM	74.31%	71.95%
Our CBM on RN50	72.79%	77.95%
Our CBM on VIT	69.70%	78.12%
Our CBM on DINO	84.39%	80.30%

D. Additional results

D.1. Sparsity evaluation.

The “Sparsity” column reports the fraction of inactive units in the learned representations, where values close to 1 indicate highly sparse codes. Lower `target_L0` values produce extremely sparse encodings (few active atoms), whereas higher `target_L0` yields denser representations (more active units). We analyze how this trade-off influences alignment measures, including geometric alignment (ρ_{geom}), activation correlation (ρ_{act}), CBM-concept coverage, regression predictability (R^2), matching entropy, and downstream F1 performance.

Overall, increasing the number of active units (i.e., reducing sparsity) improves coverage, R^2 , and sample-level F1, but leads to a loss in geometric concentration. This illustrates a trade-off between sparsity (parsimony of representation) and the semantic coverage required to approximate the CBM concept space. Consistent patterns appear across backbones: geometric alignment and entropy peak at higher sparsity levels (fewer active neurons), while activation correlation, coverage, R^2 , and F1 reach their best performance at lower sparsity, where denser codes better reconstruct the CBM concept structure.

D.2. Layer-wise evaluation of TopK SAEs.

For the ResNet-50 backbone, we conduct a layer-wise analysis by extracting features at each convolutional block and attaching a TopK SAE to each representation. The evaluated layer is reported in the “Layer” column of the table. Metrics are computed independently at every layer.

On the CUB-200 dataset, both ρ_{geom} and ρ_{act} achieve their highest values in shallower layers, whereas the remaining metrics (coverage, R^2 , entropy, and F1) achieve their best performance in deeper layers. A similar trend is observed for ImageNet, except that ρ_{act} peaks in deeper layers for this dataset. The stronger geometric alignment in early layers is likely due to their lower representational specificity: features are more generic, enabling the SAE to recover fewer but clearer latent directions. Activation correlation follows this

Table A.4. TopK SAE results (dimension = 4096) on CUB and ImageNet (IN) using ResNet-50 (R50). “target_L0” is the target activation level for TopK; “Sparsity” is the observed fraction of inactive units (higher = sparser). Missing values are marked as “-”.

Dataset-Backbone	target_L0	Sparsity	ρ_{geom}	ρ_{act}	Coverage	R^2	Entropy	F1
CUB-R50	0.0012	0.9988	0.108	0.043	0.029	0.921	6.90	0.097
	0.0024	0.9976	0.103	0.051	0.069	0.953	7.01	0.193
	0.0050	0.9951	0.098	0.062	0.238	0.968	6.84	0.249
	0.0120	0.9880	0.095	0.079	0.541	0.980	6.53	0.262
	0.0240	0.9761	0.089	0.089	0.674	0.987	6.24	0.343
	0.0500	0.9500	0.084	0.105	0.728	0.992	6.02	0.364
	0.1000	0.9382	0.087	0.122	0.735	0.989	6.02	0.355
IN-R50	0.0012	0.9988	0.160	0.051	0.039	0.766	5.42	0.142
	0.0024	0.9976	0.149	0.062	0.040	0.832	5.58	0.108
	0.0050	0.9951	0.157	0.085	0.160	0.882	6.59	0.113
	0.0120	0.9880	0.176	0.114	0.738	0.934	7.24	0.131
	0.0240	0.9761	0.172	0.130	0.914	0.980	6.84	0.130
	0.0500	0.9500	0.143	0.122	0.946	0.996	7.46	0.141
	0.1000	0.9000	0.165	0.145	0.942	0.999	7.57	0.026
CUB-VIT16B	0.0012	0.9987	0.172	0.043	0.035	0.517	7.05	0.057
	0.0024	0.9974	0.316	0.061	0.187	0.705	7.03	0.090
	0.0050	0.9948	0.249	0.062	0.377	0.711	6.69	0.139
	0.0120	0.9883	0.118	0.091	0.222	0.779	6.28	0.189
	0.0240	0.9759	0.109	0.101	0.350	0.819	5.92	0.201
	0.0500	0.9499	0.108	0.110	0.539	0.855	5.58	0.223
	0.1000	0.8997	0.107	0.120	0.669	0.893	5.41	0.239
IN-VIT16B	0.0012	0.9987	0.166	0.104	0.003	0.411	6.48	0.055
	0.0024	0.9974	0.169	0.120	0.005	0.443	6.66	0.062
	0.0050	0.9948	0.119	0.144	0.012	0.488	6.17	0.059
	0.0120	0.9883	0.081	0.175	0.042	0.559	5.45	0.044
	0.0240	0.9759	0.086	0.189	0.141	0.624	5.28	0.045
	0.0500	0.9499	0.092	0.202	0.598	0.691	5.28	0.048
	0.1000	0.8997	0.089	0.215	0.789	0.768	5.36	0.058
CUB-DINO	0.0012	0.9987	0.133	0.040	0.046	0.463	6.93	0.104
	0.0024	0.9974	0.097	0.064	0.060	0.820	6.83	0.116
	0.0050	0.9948	0.301	0.078	0.241	0.858	6.71	0.173
	0.0120	0.9883	0.262	0.079	0.493	0.892	6.48	0.206
	0.0240	0.9759	0.141	0.115	0.332	0.933	6.07	0.257
	0.0500	0.9499	0.131	0.131	0.622	0.957	5.83	0.281
	0.1000	0.8997	0.121	0.137	0.726	0.977	5.61	0.274
IN-DINO	0.0012	0.9987	0.301	0.106	0.004	0.456	6.91	0.028
	0.0024	0.9974	0.236	0.129	0.007	0.511	6.80	0.032
	0.0050	0.9948	0.149	0.158	0.012	0.588	6.15	0.027
	0.0120	0.9883	0.107	0.187	0.026	0.685	5.64	0.019
	0.0240	0.9759	0.110	0.207	0.136	0.767	5.50	0.020
	0.0500	0.9499	0.105	0.226	0.505	0.819	5.37	0.023
	0.1000	0.8997	0.092	0.235	0.800	0.868	5.24	0.017

trend on CUB, but on ImageNet the CBM concepts are more fine-grained, making deeper layers better aligned with them.

Table A.5. Layer-wise evaluation of TopK SAEs (dimension indicated per layer) trained on CUB and ImageNet (IN) with ResNet-50 (R50) features. Each SAE exhibits high sparsity (≈ 0.995). Metrics assess geometric and activation alignment (ρ_{geom} , ρ_{act}), coverage of CBM concepts, predictability (R^2), entropy, and downstream F1 performance.

Dataset-Backbone	Layer (Dim)	Sparsity	ρ_{geom}	ρ_{act}	Coverage	R^2	Entropy	F1
CUB-R50	Layer 1 (512)	0.994	0.105	0.065	0.012	0.491	6.25	0.120
	Layer 2 (1024)	0.995	0.116	0.061	0.003	0.597	6.19	0.115
	Layer 3 (2048)	0.995	0.067	0.058	0.006	0.672	6.19	0.266
	Layer 4 (4096)	0.995	0.098	0.063	0.245	0.968	6.85	0.221
IN-R50	Layer 1 (512)	0.994	0.357	0.012	0.021	0.133	1.78	0.019
	Layer 2 (1024)	0.995	0.226	0.017	0.004	0.183	3.39	0.074
	Layer 3 (2048)	0.995	0.140	0.038	0.027	0.707	7.82	0.095
	Layer 4 (4096)	0.995	0.156	0.086	0.194	0.881	6.71	0.052

D.3. Expansion factor analysis of TopK SAEs.

We also evaluate the effect of the expansion factor across all backbones for both CUB and ImageNet. The tested expansion factors, reported in the “Expansion” column, range from

$\times 1$ to $\times 8$, with the corresponding SAE latent dimensions shown in brackets.

Across architectures and datasets, we observe consistent behavior: geometric alignment (ρ_{geom}) and activation correlation (ρ_{act}) are strongest at lower expansion factors, corresponding to fewer distinct concept directions. Conversely, larger latent spaces, achieved through higher expansion factors, tend to improve coverage, R^2 , entropy, and F1, indicating that increased capacity helps capture a broader and more detailed concept space.

Table A.6. Effect of the expansion factor on TopK SAEs trained with ResNet-50 (R50) features for CUB and ImageNet (IN). Increasing the expansion factor enlarges the latent space dimensionality. Metrics evaluate geometric and activation alignment ($\rho_{\text{geom}}, \rho_{\text{act}}$), concept coverage, predictability (R^2), entropy, and downstream precision and F1.

Dataset-Backbone	Expansion	Sparsity	ρ_{geom}	ρ_{act}	Coverage	R^2	Entropy	Precision	F1
CUB-R50	$\times 1$ (2048)	0.995	0.102	0.122	0.051	0.890	6.684	0.177	0.220
	$\times 2$ (4096)	0.995	0.098	0.102	0.237	0.969	6.819	0.178	0.218
	$\times 4$ (8192)	0.995	0.095	0.095	0.617	1.00	6.86	0.243	0.299
	$\times 8$ (16384)	0.995	0.074	0.074	0.898	1.00	6.97	0.310	0.361
IN-R50	$\times 1$ (2048)	0.995	0.175	0.165	0.035	0.818	6.186	0.135	0.115
	$\times 2$ (4096)	0.995	0.156	0.145	0.194	0.881	6.71	0.141	0.129
	$\times 4$ (8192)	0.995	0.161	0.147	0.721	0.935	8.05	0.121	0.121
	$\times 8$ (16384)	0.995	0.148	0.133	0.939	0.967	8.40	0.125	0.133
CUB-ViT	$\times 1$ (768)	0.9948	0.158	0.073	0.052	0.627	6.77	0.096	0.125
	$\times 2$ (1536)	0.9948	0.249	0.062	0.377	0.711	6.69	0.108	0.139
	$\times 4$ (3072)	0.9951	0.131	0.053	0.280	0.803	5.41	0.144	0.180
	$\times 8$ (6144)	0.9950	0.109	0.057	0.677	0.990	6.48	0.157	0.195
IN-ViT	$\times 1$ (768)	0.9948	0.077	0.180	0.004	0.387	5.75	0.046	0.046
	$\times 2$ (1536)	0.9948	0.116	0.145	0.012	0.491	6.27	0.065	0.061
	$\times 4$ (3072)	0.9951	0.103	0.124	0.055	0.583	6.37	0.095	0.070
	$\times 8$ (6144)	0.9950	0.081	0.110	0.797	0.712	6.45	0.153	0.092
IN-DINO (CUB-DINO)	$\times 1$ (768)	0.9948	0.085	0.086	0.045	0.774	6.81	0.116	0.148
	$\times 2$ (1536)	0.9948	0.301	0.078	0.241	0.858	6.71	0.144	0.173
	$\times 4$ (3072)	0.9951	0.331	0.061	0.561	0.931	6.62	0.171	0.212
	$\times 8$ (6144)	0.9950	0.162	0.054	0.673	0.995	6.88	0.211	0.246
IN-DINO	$\times 1$ (768)	0.9948	0.131	0.189	0.005	0.459	5.98	0.012	0.014
	$\times 2$ (1536)	0.9948	0.114	0.119	0.028	0.409	5.44	0.076	0.060
	$\times 4$ (3072)	0.9951	0.151	0.133	0.058	0.696	6.32	0.056	0.048
	$\times 8$ (6144)	0.9950	0.119	0.129	0.610	0.821	6.32	0.113	0.076

E. Application: Analysis of the SAE representation on Husky Vs Wolf dataset

To further investigate how SAEs and CBMs encode semantic information, we conduct a focused experiment on a two-class subset of ImageNet composed of *Husky* and *Wolf* images, following the experimental setting proposed in [29]. We rely on the annotated concept set provided in [12], which offers image-level and class-level semantic attributes for these two classes. These annotations serve as ground-truth concepts for the CBM branch.

We begin by training a ResNet-50 backbone for binary classification on the Husky/Wolf subset. After training the classifier, we attach both a TopK SAE and a CBM module to the final convolutional block of the frozen backbone. The CBM branch predicts the concept vector through its concept-extractor matrix W_c , while the SAE learns a dictionary D that provides a sparse generative decomposition of the features. This parallel construction allows us to analyze to what extent the learned SAE atoms align with 'human-based

words' CBM concepts.

Concept Matching Between SAE Atoms and CBM Concepts. To quantify semantic alignment between the SAE and the CBM, we compute a concept–dictionary similarity matrix S defined as

$$S_{i,j} = \text{corr}(D_j, W_{c,i}),$$

where D_j denotes the j -th dictionary atom of the SAE and $W_{c,i}$ the i -th concept direction learned by the CBM. For each atom j , we identify its most associated concept by selecting

$$\hat{i}(j) = \arg \max_i |S_{i,j}|.$$

This establishes a direct one-to-one correspondence between SAE atoms and CBM concepts. In addition to matching dictionary atoms, we also align the latent representations of the SAE with CBM concepts. For each latent embedding $Z_{\cdot,j}^{\text{SAE}}$, we first identify the most influential atom by selecting the dictionary element that exhibits the strongest activation for that sample. Using the atom-to-concept assignment described above, we then propagate this match to the latent representations. This yields a consistent alignment across three elements: the dictionary atoms D_j , the CBM concept directions $W_{c,i}$, and the latent activations $Z_{\cdot,j}^{\text{SAE}}$. At this stage, both the SAE latent space and its dictionary are mapped onto the CBM semantic space, enabling a direct comparison between the representations learned by the two models.

UMAP Visualization of SAE Dictionary Structure. Figure A.4 shows a UMAP projection of the SAE dictionary atoms, providing a global view of their geometric organization. To further analyze semantic alignment, we compute cosine similarities between selected CBM concepts and all SAE atoms. The UMAP plots reveal that only a small subset of atoms exhibits strong similarity to any given concept, while most atoms show weak or diffuse alignment. This indicates that a limited number of dictionary atoms capture the majority of the shared semantic signal between the SAE and the CBM, whereas many other atoms correspond to fine-grained or heterogeneous features that do not map cleanly onto human-annotated concepts.

Concept Distribution Across Classes. To quantify how the two classes differ in terms of their concept activations, we assign to each sample the most influential concept determined via its highest correlation with the SAE dictionary as described above. This enables us to compute per-class histograms, shown in Figure A.5. These histograms highlight strong biases: certain concepts appear much more frequently in Husky images than in Wolf images, and vice versa. Such

asymmetries echo known dataset biases in the Husky/Wolf classification task (e.g., wolves often appear in snowy or wild backgrounds whereas huskies appear in urban or domestic contexts). This demonstrates that the SAE+CBM analysis pipeline is able to reveal and disentangle these latent dataset biases without any explicit guidance, reinforcing the interpretability benefits of combining sparse generative modeling with concept supervision.

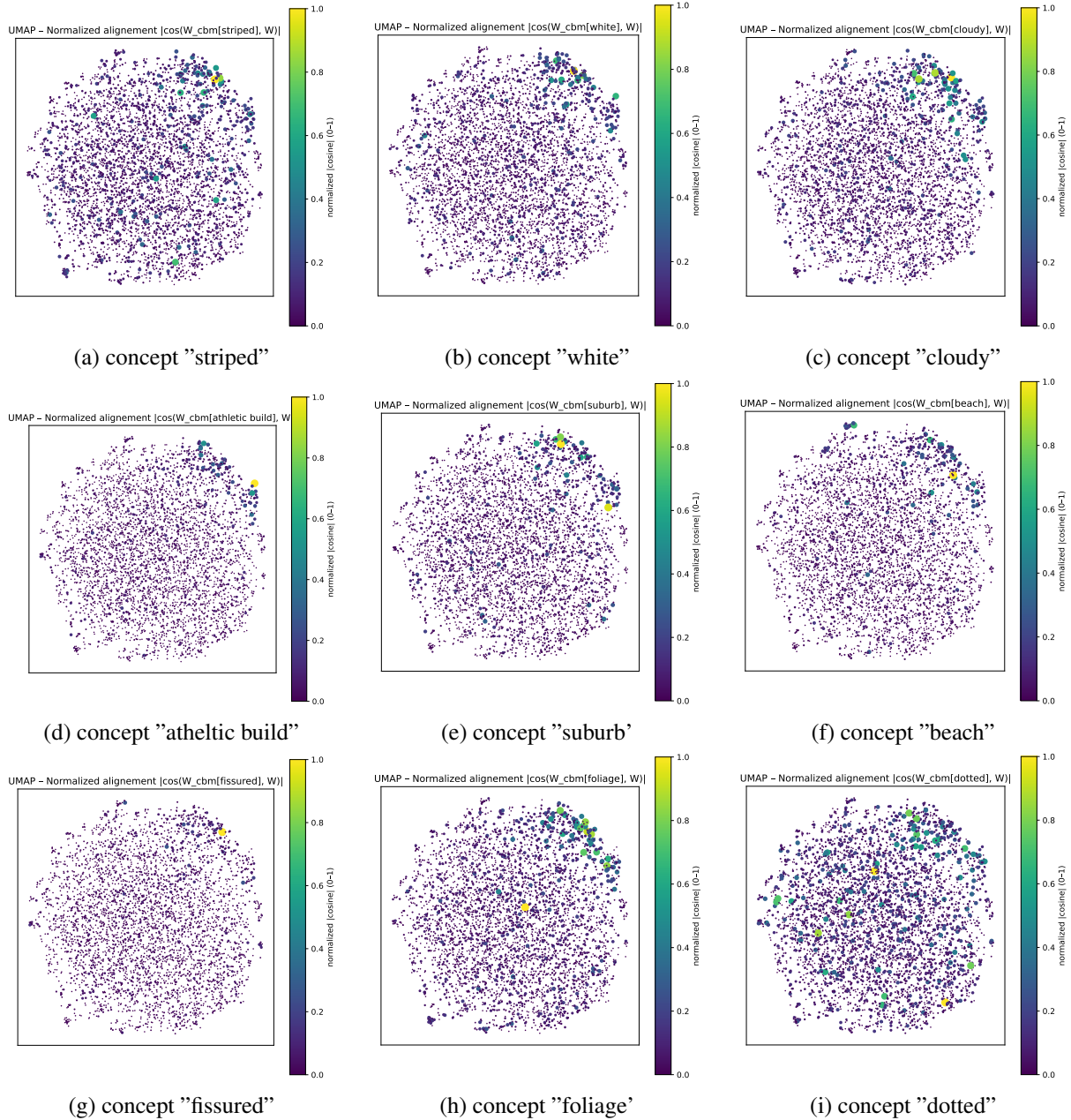


Figure A.4. Cosine similarities between selected CBM concepts and all SAE dictionary atoms, visualized through UMAP. Strong responses concentrate around a limited number of atoms, suggesting that only a small fraction of SAE directions encode concepts shared with the CBM.

Concept Distribution Comparison Husky vs Wolf

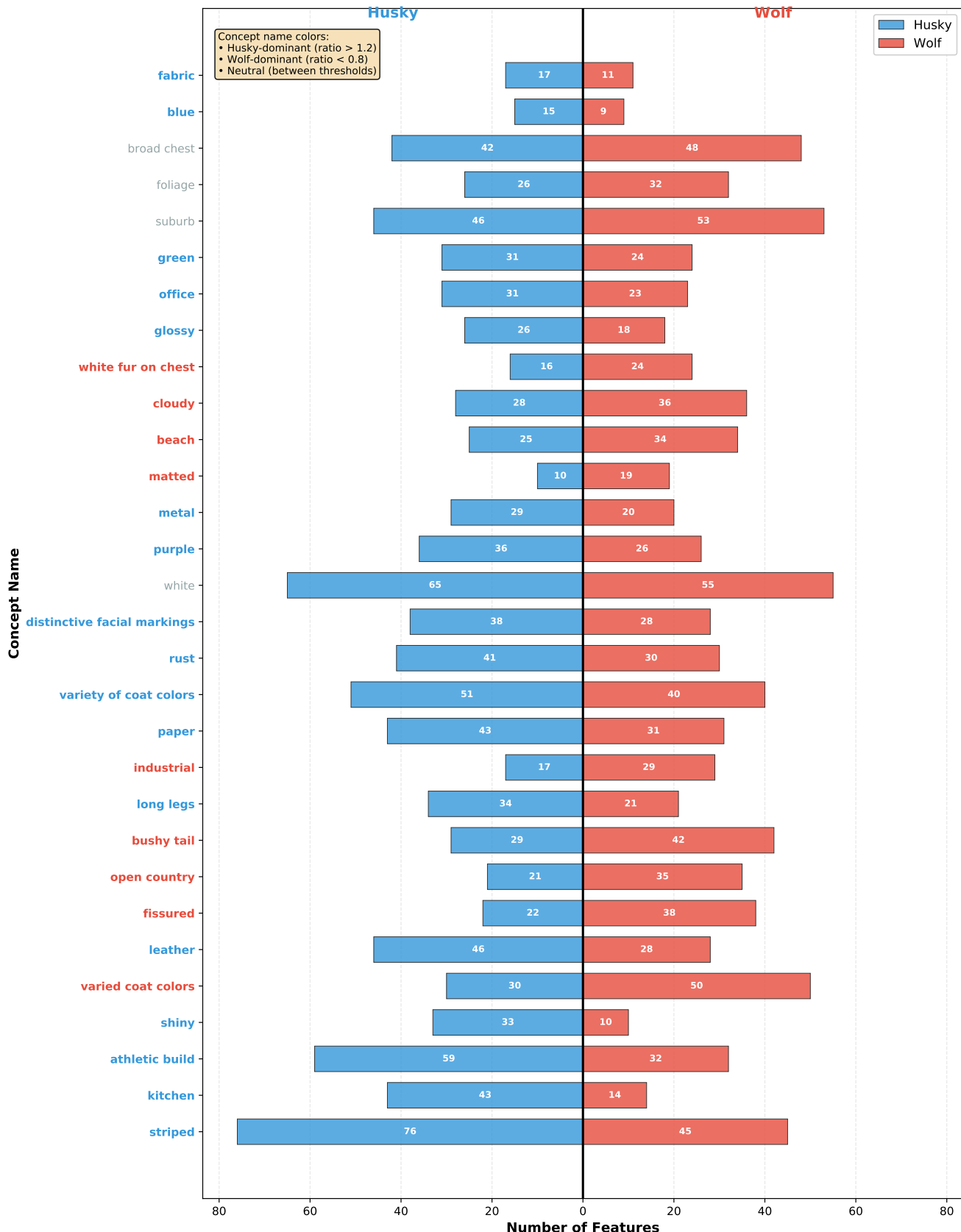


Figure A.5. Class-wise concept histograms for Husky and Wolf images. Each sample is assigned the concept with maximum correlation to its SAE representation, revealing clear concept-frequency biases between the two classes.